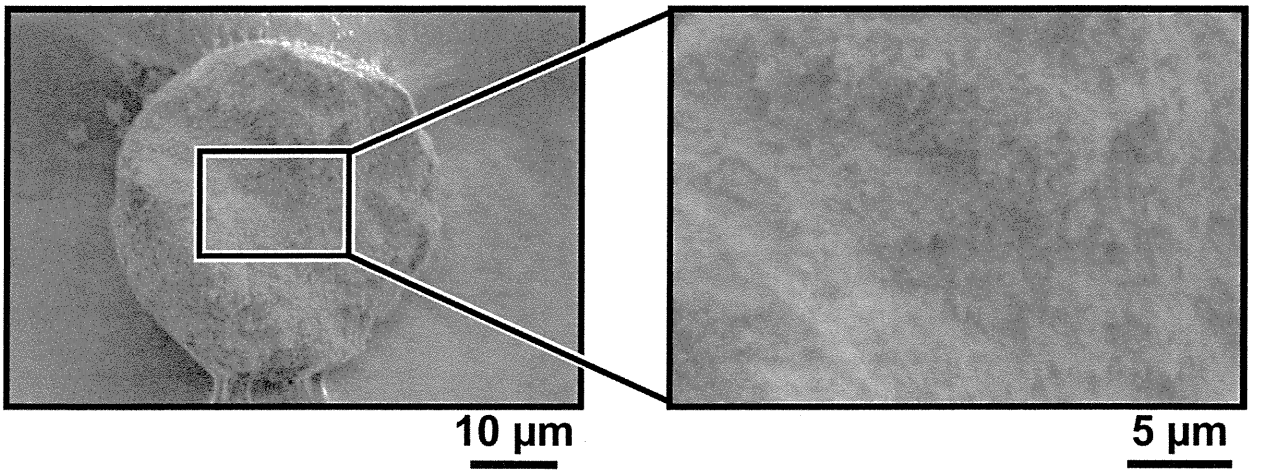

FIGURE 3. SEM photographs of cross-sections of samples after heat treatment at 1100°C.

owing to the production of lactic acid.[38] The SBF was shaken at a rate of 120 strokes/min using a stroke length of 3 cm. The samples were soaked for up to 21 days, because the radioactivity of ^{90}Y decays to a negligible level after 21 days. An inductively coupled plasma (ICP) atomic emission spectrometer (Optima 2000DV, PerkinElmer Co., Germany) was used to determine the concentrations of yttrium and phosphorus released from the microspheres into SBF-6 or SBF-7. The fraction of yttrium released from the microspheres was calculated using the following formula.

$$\text{Released fraction} = \frac{\text{Molar quantity of yttrium released from the microsphere into the SBF (mol)}}{\text{Total molar quantity of yttrium contained in the microsphere (mol)}}$$

RESULTS

Figure 1 shows XRD patterns of samples before and after heat treatment at different temperatures. The untreated sample exhibited a halo, indicating that its structure was amorphous. Several peaks of tetragonal YPO_4 with the xenotime structure (PDF File No. 11-0254) were clearly observed after heat treatment at temperatures above 700°C. With a further increase in heat treatment temperature to 1500°C, the structure of the sample remained dehydrated YPO_4 with tetragonal xenotime-type structure,[35] but the diffraction peaks became more intense and narrower, indicating crystal growth of YPO_4 with increasing heat treatment temperature.

Figure 2 shows SEM photographs of samples before and after heat treatment at different temperatures. Microspheres around 25 μm in diameter with smooth surfaces were successfully obtained by the present method, although their diameters ranged from 10 to 80 μm. The surface smoothness of the microspheres was improved slightly by heat treatment at 700°C or 1100°C. This might be attributed to partial sintering of YPO_4 by the heat treatment. With heat treatment at 1500°C, the surface of the microspheres became rather rough, and remarkable aggregation of the microspheres occurred. It seems plausible that the microspheres heat-treated at higher temperatures will show higher chemical durability in the human body, because sintering of YPO_4 will proceed at higher temperatures. However, the rough surface and aggregation of the microspheres are unfavorable for clinical application of intra-arterial therapy. Therefore, we considered that the maximum useful heat treatment temperature is 1100°C, and an *in vitro* chemical durability test was conducted for the microspheres heat-treated at 1100°C in this study. Figure 3 shows SEM photographs of cross-sections of these microspheres. Figures 2 and 3 show that both the inside and the outer surface of the microspheres heat-treated at 1100°C were dense.

Figure 4 shows the concentrations of yttrium and phosphorus released from the microspheres heat-treated at 1100°C into SBF-6 or SBF-7 after immersion for 21 days, in comparison with those of the original SBF without soaking of the microspheres. The concentrations of yttrium released from the microspheres into SBF-6 and SBF-7 were as low as 0.3 mg/g, which is almost the same as the yttrium concentration of the original SBF without microsphere soaking [Figure 4(a)]. It is interesting to note that the concentrations of phosphorus in SBF-6 and SBF-7 in which the microspheres were soaked for 21 days were slightly lower than those of the original SBF [Figure 4(b)]. There is possibility that YPO_4 precipitate in SBF solutions if small amount of yttrium is released from the microspheres, but we were not able to confirm any precipitation visually in either SBF-6 and SBF-7 after the chemical durability test. This suggests that the microspheres heat-treated at 1100°C released

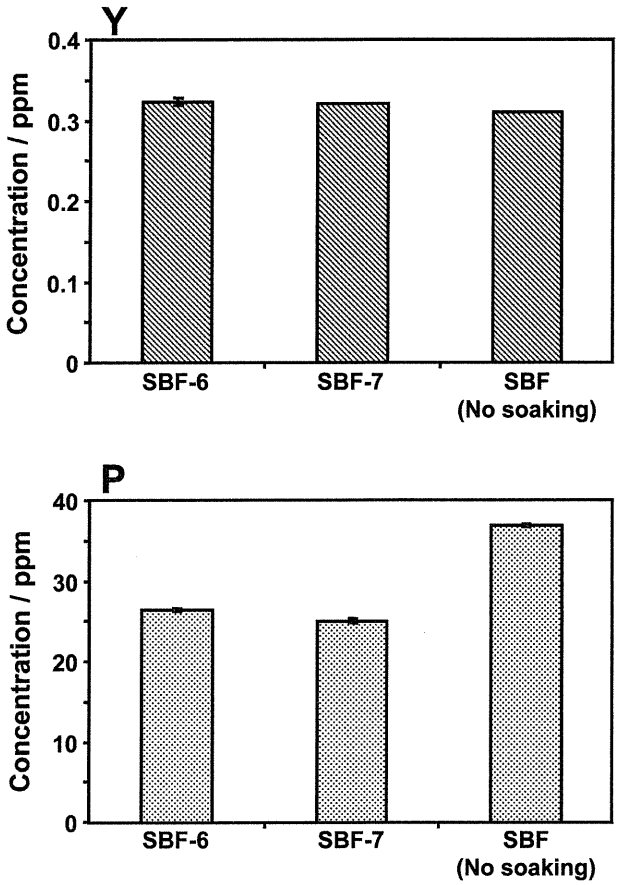

FIGURE 4. Concentrations of yttrium and phosphorus released from the microspheres heat-treated at 1100°C into SBF-6 or SBF-7 after 21 days, in comparison with those of the original SBF without soaking of the microspheres.

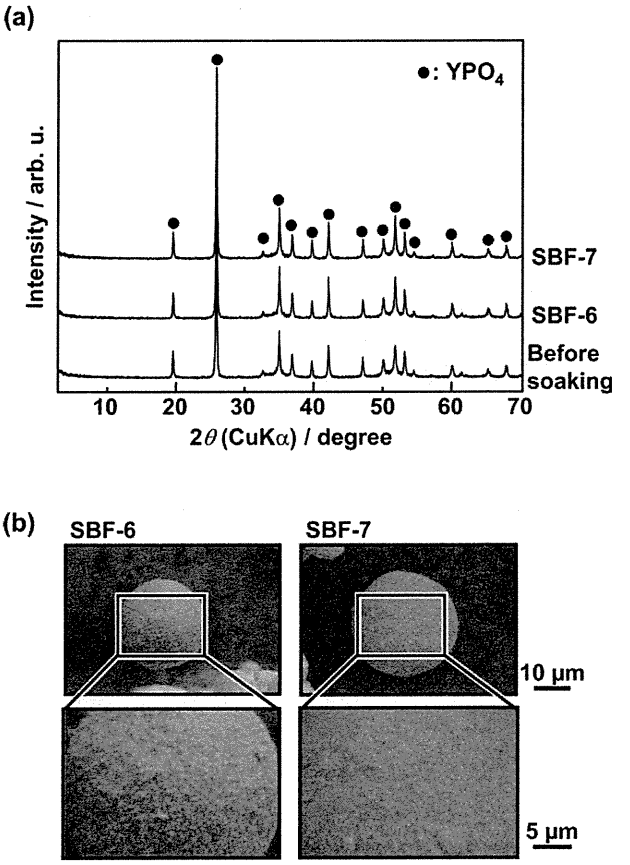

FIGURE 5. XRD patterns (a) and SEM photographs (b) of the microspheres heat-treated at 1100°C before and after soaking in SBF-6 or SBF-7 for 21 days.

hardly any yttrium into either SBF-6 and SBF-7 after 21 days, and a small amount of phosphorus might adsorb onto the surfaces of the microspheres and/or react with the microspheres.

Figure 5 shows the XRD patterns (a) and SEM photographs (b) of the microspheres heat-treated at 1100°C before and after soaking in SBF-6 and SBF-7 for 21 days. No appreciable change was observed in the XRD patterns and the SEM photographs of the microspheres after soaking in either of the SBF solutions. Figure 6 shows the FT-IR diffusive spectra of the microspheres heat-treated at 1100°C before and after soaking in SBF-6 and SBF-7 for 21 days. The microspheres before soaking showed several bands assigned to PO_4.[39,40] The bands at around 3500 cm^{-1} and 1630 cm^{-1}, which are assigned to H_2O,[39,40] appeared after the microspheres were soaked in SBF-6 or SBF-7. This might be attributed to partial hydration of the microspheres' surfaces due to the chemical durability test. The intensity of the bands at around 1300 and 3000 cm^{-1} increased after the chemical durability test. These two bands are assigned to PO_4 and CH_3, respectively.[39-41] This result suggests adsorption of a small amount of phosphorus-containing organic compounds onto the surfaces of the microspheres, although the detailed structure of the compounds is unclear.

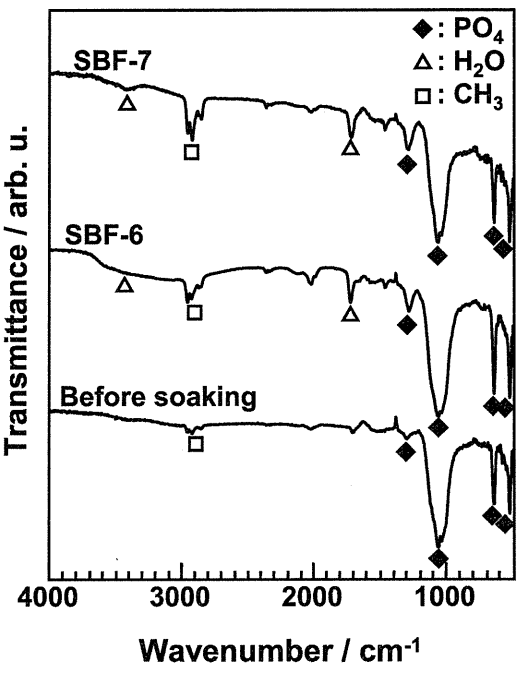

FIGURE 6. FT-IR diffusive spectra of samples before and after soaking in SBF-6 or SBF-7 for 21 days.

TABLE 1. Fraction of Yttrium Released from the Samples into SBF-6, SBF-7, and Saline Solutions Buffered at pH = 6 or 7 at 36.5°C for 21 days

Sample	Immersion Fluid	
	SBF-6	SBF-7
Present YPO_4 microspheres	2.5×10^{-5}	2.5×10^{-5}
Hollow Y_2O_3 microspheres[31]	1.8×10^{-3}	1.3×10^{-3}
Porous Y_2O_3 microparticles[32]	5.6×10^{-3}	5.2×10^{-3}
	Saline solutions buffered at pH = 6	Saline solutions buffered at pH = 7
Dense Y_2O_3 microspheres[30]	4×10^{-3}	2×10^{-3}
YPO_4-Y_2O_3 microspheres[30]	2.5×10^{-3}	undetectable level
Y_2O_3-Al_2O_3-SiO_2 (TheraSphere®-type) glass[30]	9×10^{-3}	3×10^{-3}

Also, it is consistent with the results of the *in vitro* chemical durability test, indicating that the concentrations of phosphorus in SBF-6 and SBF-7 in which the microspheres were soaked for 21 days were slightly lower than those of the original SBF (see Figue 4). According to these results, we can conclude that the present microspheres heat-treated at 1100°C are quite chemically stable under acidic and neutral SBF solutions.

DISCUSSION

We examined the durability of the heat-treated microspheres by immersion for 21 days in SBF (Figure 4). Note, however, that the radioactivity of ^{32}P decays to a negligible level only after 112 days, and hence, it might be advisable to evaluate the chemical durability of the microspheres for a longer period of 112 days. However, we can expect that the present YPO_4 microspheres would show high chemical durability for long periods such as 112 days because we confirmed that microspheres consisting of YPO_4 and Y_2O_3 (YPO_4–Y_2O_3 microspheres) showed excellent chemical durability for 112 days in saline with both pH = 6 and pH = 7 in our previous study.[30] Moreover, the activity product of YPO_4 is reportedly as low as $10^{-24.76}$ at 25 ± 1°C.[42]

In Table I, the fraction of yttrium released from the present YPO_4 microparticles is compared with that of previously reported samples. The present YPO_4 microspheres showed smaller released yttrium fractions than the previously reported samples, although the chemical durability of some samples (dense Y_2O_3 microspheres, YPO_4–Y_2O_3 microspheres, and Y_2O_3–Al_2O_3–SiO_2 [TheraSphere®-type] glass) was evaluated in saline solutions buffered at pH = 6 or 7. Particularly, we noted that the fraction of yttrium released from the present YPO_4 microspheres was much smaller than that from TheraSphere®-type glass and dense Y_2O_3 microspheres, which showed no acute toxicity in animal tests,[43] indicating that the chemical durability of the present YPO_4 microspheres is high enough for clinical application in intra-arterial radiotherapy.

CONCLUSIONS

YPO_4 microspheres around 25 μm in diameter with smooth surfaces were successfully obtained by cooling and solidifying gelatin droplets containing yttrium phosphate precursor precipitates in a water-in-oil emulsion and then heat-treating them at 1100°C. The *in vitro* chemical durability of the heat-treated microspheres in a simulated body fluid at pH = 6 and 7 was high enough for clinical application of intra-arterial radiotherapy. We believe that the present YPO_4 microspheres are useful for intra-arterial radiotherapy of cancer, since they have smooth surfaces and can be activated to β-emitters by neutron bombardment.

REFERENCES

1. Nicolay NH, Berry DP, Sharma RA. Liver metastases from colorectal cancer: Radioembolization with systemic therapy. Nat Rev Clin Oncol 2009;6:687–697.
2. Kerr SH, Kerr DJ. Novel treatments for hepatocellular cancer. Cancer Lett 2009;286:114–120.
3. Hyatt MJ, Day DE. Glass properties in the yttria-alumina-silica system. J Am Ceram Soc 1987;70:283–287.
4. Ehrhardt GJ, Day DE. Therapeutic use of ^{90}Y microspheres. J Nucl Med 1987;14:233–242.
5. Erbe EM, Day DE. Chemical durability of Y_2O_3-Al_2O_3-SiO_2 glasses for the in vivo delivery of beta radiation. J Biomed Mater Res 1993;27:1301–1308.
6. Meade VM, Burton MA, Gray BN, Self GW. Distribution of different sized microspheres in experimental hepatic tumors. Eur J Cancer Clin Oncol 1987;23:37–41.
7. Burton MA, Gray BN, Klemp PF, Kelleher DK, Hardy N. Selective internal radiation therapy: Distribution of radiation in the liver. Eur J Cancer Clin Oncol 1989;25:1487–1491.
8. Gray BN, Anderson JE, Burton MA, Vanhazel G, Codde J, Morgan C, Klemp P. Regression of liver metastases following treatment with Y-90 microspheres. Aust N Z J Surg 1992;62:105–110.
9. Shepherd FA, Rotstein LE, Houle S, Yip TCK, Paul K, Sniderman KW. A phase-I dose escalation trial of Y-90 microspheres in the treatment of primary hepatocellular-carcinoma. Cancer 1992;70: 2250–2254.
10. Lau WY, Leung WT, Ho S, Leung NWY, Chan M, Lin J, Metreweli C, Johnson P, Li AKC. Treatment of inoperable hepatocellular carcinoma with intrahepatic arterial Y-90 microspheres: A phase-I and phase-II study. Br J Cancer 1994;70:994–999.
11. Lau WY, Ho S, Leung TWT, Chan M, Ho R, Johnson PJ, Li AKC. Selective internal radiation therapy for nonresectable hepatocellular carcinoma with intraarterial infusion of ^{90}yttrium microspheres. Int J Radiat Oncol Biol Phys 1998;40:583–592.
12. Campbell AM, Bailey IH, Burton MA. Analysis of the distribution of intra-arterial microspheres in human liver following hepatic yttrium-90 microsphere therapy. Phys Med Biol 2000;45:1023–1033.
13. Stubbs RS, Cannan RJ, Mitchell AW. Selective internal radiation therapy with ^{90}yttrium microspheres for extensive colorectal liver metastases. J Gastro Surg 2001;5:294–302.
14. Gray B, Van Hazel G, Hope M, Burton M, Moroz P, Anderson J, Gebski V. Randomised trial of SIR-Spheres® plus chemotherapy vs. chemotherapy alone for treating patients with liver metastases from primary large bowel cancer. Ann Oncol 2001;12: 1711–1720.
15. Salem R, Thurston KG, Carr BI, Goin JE, Geschwind JFH. Yttrium-90 microspheres: Radiation therapy for unresectable liver cancer. J Vasc Interv Radiol 2002;13:S223–S229.

16. Kennedy AS, Nutting C, Coldwell D, Gaiser J, Drachenberg C. Pathologic response and microdosimetry of Y-90 microspheres in man: Review of four explanted whole livers. Inter J Radiat Oncol Biol Phys 2004;60:1552–1563.
17. Geschwind JFH, Salem R, Carr BI, Soulen MC, Thurston KG, Goin KA, Van Buskirk M, Roberts CA, Goin JE. Yttrium-90 microspheres for the treatment of hepatocellular carcinoma. Gastroenterology 2004;127:S194–S205.
18. Salem R, Lewandowski R, Roberts C, Goin J, Thurston K, Abouljoud M, Courtney A. Use of yttrium-90 glass microspheres (TheraSphere) for the treatment of unresectable hepatocellular carcinoma in patients with portal vein thrombosis. J Vasc Interv Radiol 2004;15:335–345.
19. Salem R, Lewandowski RJ, Atassi B, Gordon SC, Gates VL, Barakat O, Sergie Z, Wong CYO, Thurston KG. Treatment of unresectable hepatocellular carcinoma with use of Y-90 microspheres (TheraSphere): Safety, tumor response, and survival. J Vasc Interv Radiol 2005;16:1627–1639.
20. Murthy R, Nunez R, Szklaruk J, Erwin W, Madoff DC, Gupta S, Ahrar K, Wallace MJ, Cohen A, Coldwell DM, Kennedy AS, Hicks ME. Yttrium-90 microsphere therapy for hepatic malignancy: Devices, indications, technical considerations, and potential complications. Radiographics 2005;25:S41–S56.
21. Murthy R, Xiong H, Nunez R, Cohen AC, Barron B, Szklaruk J, Madoff DC, Gupta S, Wallace MJ, Ahrar K, Hicks ME. Yttrium 90 resin microspheres for the treatment of unresectable colorectal hepatic metastases after failure of multiple chemotherapy regimens: Preliminary results. J Vasc Interv Radiol 2005;16:937–945.
22. Avila MA, Berasain C, Sangro B, Prieto J. New therapies for hepatocellular carcinoma. Oncogene 2006;25:3866–3884.
23. Salem R, Thurston KG. Radioembolization with ^{90}Yttrium microspheres: A state-of-the-art brachytherapy treatment for primary and secondary liver malignancies: Part 1: Technical and methodologic considerations. J Vasc Interv Radiol 2006;17:1251–1278.
24. Salem R, Thurston KG. Radioembolization with ^{90}Yttrium microspheres: A state-of-the-art brachytherapy treatment for primary and secondary liver malignancies: Part 2: Special topics. J Vasc Interv Radiol 2006;17:1425–1439.
25. Salem R, Thurston KG. Radioembolization with yttrium-90 microspheres: A state-of-the-art brachytherapy treatment for primary and secondary liver malignancies: Part 3: Comprehensive literature review and future direction. J Vasc Interv Radiol 2006;17:1571–1593.
26. Kennedy AS, Coldwell D, Nutting C, Murthy R, Wertman DE, Loehr SP, Overton C, Meranze S, Niedzwiecki J, Sailer S. Resin Y-90-microsphere brachytherapy for unresectable colorectal liver metastases: Modern USA experience. Int J Radiat Oncol Biol Phys 2006;65:412–425.
27. Kennedy A, Nag S, Salem R, Murthy R, McEwan AJ, Nutting C, Benson A, Espat J, Bilbao JI, Sharma RA, Thomas JP, Coldwell D. Recommendations for radioembolization of hepatic malignancies using yttrium-90 microsphere brachytherapy: A consensus panel report from the Radioembolization Brachytherapy Oncology Consortium. Int J Radiat Oncol Biol Phys 2007;68:13–23.
28. Hilgard P, Hamami M, El Fouly A, Scherag A, Muller S, Ertle J, Heusner T, Cicinnati VR, Paul A, Bockisch A, Gerken G, Antoch G. Radioembolization with yttrium-90 glass microspheres in hepatocellular carcinoma: European experience on safety and long-term survival. Hepatology 2010;52:1741–1749.
29. Day DE, Day TE. Radiotherapy glasses. In: Hench LL, Wilson J, editors. An Introduction to Bioceramics. Singapore: World Scientific; 1993. pp 305–317.
30. Kawashita M, Shineha R, Kim HM, Kokubo T, Inoue Y, Araki N, Nagata Y, Hiraoka M, Sawada Y. Preparation of ceramic microspheres for in situ radiotherapy of deep-seated cancer. Biomaterials 2003;24:2955–2963.
31. Kawashita M, Takayama Y, Kokubo T, Takaoka GH, Araki N, Hiraoka M. Enzymatic preparation of hollow yttrium oxide microspheres for in situ radiotherapy of deep-seated cancer. J Am Ceram Soc 2006;89:1347–1351.
32. Kawashita M, Matsui N, Li Z, Miyazaki T. Preparation of porous yttrium oxide microparticles by gelation of ammonium alginate in aqueous solution containing yttrium ions. J Mater Sci Mater Med 2010;21:1837–1843.
33. Gao W, Liu L, Teng GJ, Feng GS, Tong GS, Gao NR. Internal radiotherapy using ^{32}P colloid or microsphere for refractory solid tumors. Ann Nucl Med 2008;22:653–660.
34. Wang XM, Yin ZY, Yu RX, Peng YY, Liu PG, Wu GY. Preventive effect of regional radiotherapy with phosphorus-32 glass microspheres in hepatocellular carcinoma recurrence after hepatectomy. World J Gastroenterol 2008;14:518–523.
35. Di W, Wang X, Chen B, Lu S, Zhao X. Effect of OH^- on the luminescent efficiency and lifetime of Tb^{3+}-doped yttrium orthophosphate synthesized by solution precipitation. J Phys Chem B 2005; 109:13154–13158.
36. Miyazaki T, Kai T, Ishida E, Kawashita M, Hiraoka M. Fabrication of yttria microcapsules for radiotherapy from water/oil emulsion. J Ceram Soc Jpn 2010;118:479–482.
37. Cho SB, Nakanishi K, Kokubo T, Soga N, Ohtsuki C, Nakamura T, Kitsugi T, Yamamuro T. Dependence of apatite formation on silica gel on its structure: Effect of heat treatment. J Am Ceram Soc 1995;78:1769–1774.
38. Hiraoka M, Hahn GM. Comparison between tumor pH and cell sensitivity to heat in RIF-1 tumors. Cancer Res 1989;49:3734–3736.
39. Hezel A, Ros SD. Forbidden transitions in the infra-red spectra of tetrahedral anions—III. Spectra-structure correlations in perchlorates, sulphates and phosphates of the formula MXO_4. SpectrochimActa 1966;22:1949–1961.
40. Lucas S, Champion E, Bregiroux D, Bernache-Assollant D, Audubert F. Rare earth phosphate powders $RePO_4{\cdot}nH_2O$ (Re=La, Ce or Y)—Part I. Synthesis and characterization. J Solid State Chem 2004;177:1302–1311.
41. Briche S, Zambon D, Chadeyron G, Boyer D, Dubois M, Mahiou R. Comparison of yttrium polyphosphate $Y(PO_3)_3$ prepared by sol–gel process and solid state synthesis. J Sol-Gel Sci Technol 2010;55:41–51.
42. Firsching FH, Brune SN. Solubility products of the trivalent rare-earth phosphates. J Chem Eng Data 1991;36:93–95.
43. Kawashita M. Ceramic microspheres for biomedical applications. Int J Appl Ceram Tech 2005;2:173–183.

Structure
Article

Crystal Structures of the Armadillo Repeat Domain of Adenomatous Polyposis Coli and Its Complex with the Tyrosine-Rich Domain of Sam68

Ella Czarina Morishita,[1] Kazutaka Murayama,[1,2] Miyuki Kato-Murayama,[1] Yoshiko Ishizuka-Katsura,[1] Yuri Tomabechi,[1] Tomoatsu Hayashi,[3] Takaho Terada,[1] Noriko Handa,[1] Mikako Shirouzu,[1] Tetsu Akiyama,[3] and Shigeyuki Yokoyama[1,4,*]
[1]RIKEN Systems and Structural Biology Center, 1-7-22 Suehiro-cho, Tsurumi, Yokohama 230-0045, Japan
[2]Division of Biomedical Measurements and Diagnostics, Graduate School of Biomedical Engineering, Tohoku University, 2-1 Seiryo-machi, Aoba, Sendai 980-8575, Japan
[3]Laboratory of Molecular and Genetic Information, Institute of Molecular and Cellular Biosciences
[4]Department of Biophysics and Biochemistry, Graduate School of Science
The University of Tokyo, 7-3-1 Hongo, Bunkyo, Tokyo 113-0033, Japan
*Correspondence: yokoyama@biochem.s.u-tokyo.ac.jp
DOI 10.1016/j.str.2011.07.013

SUMMARY

Adenomatous polyposis coli (APC) is a tumor suppressor protein commonly mutated in colorectal tumors. APC plays important roles in Wnt signaling and other cellular processes. Here, we present the crystal structure of the armadillo repeat (Arm) domain of APC, which facilitates the binding of APC to various proteins. APC-Arm forms a superhelix with a positively charged groove. We also determined the structure of the complex of APC-Arm with the tyrosine-rich (YY) domain of the Src-associated in mitosis, 68 kDa protein (Sam68), which regulates TCF-1 alternative splicing. Sam68-YY forms numerous interactions with the residues on the groove and is thereby fixed in a bent conformation. We assessed the effects of mutations and phosphorylation on complex formation between APC-Arm and Sam68-YY. Structural comparisons revealed different modes of ligand recognition between the Arm domains of APC and other Arm-containing proteins.

INTRODUCTION

Adenomatous polyposis coli (APC) was originally identified as the gene responsible for the onset of familial adenomatous polyposis (FAP) (Bodmer et al., 1987; Leppert et al., 1987). Patients with FAP carry germline mutations of the *apc* gene, and are predisposed toward developing multiple colorectal polyps, which may progress to malignant carcinomas. Truncating mutations in *apc* were characterized in patients with sporadic colorectal cancers, which represent approximately 85% of human colorectal cancers (Ashton-Rickardt et al., 1989; Groden et al., 1991). Studies in mice demonstrated that heterozygotes carrying a truncated *apc* gene develop tumors in the intestine (Fodde et al., 1994; Oshima et al., 1995, 1997).

The *apc* gene encodes a large 310 kDa protein that can be divided into the N-terminal, central, and C-terminal regions (Figure 1A). The N-terminal region contains an oligomerization domain, followed by the armadillo repeat (Arm) domain. The C-terminal region contains the basic domain, and the binding sites for end-binding protein 1 (EB1) and discs-large (DLG) protein. The central region contains three 15 amino acid repeats, followed by seven 20 amino acid repeats. The former binds to β-catenin, whereas the latter both binds and downregulates β-catenin (Munemitsu et al., 1995; Rubinfeld et al., 1993; Su et al., 1993). β-Catenin is a well-established key effector of the Wnt-signaling pathway. In the presence of a Wnt signal, or in the absence of APC, β-catenin accumulates in the cytoplasm, then translocates into the nucleus, where it associates with the members of the T cell factor (TCF) and lymphoid enhancer factor (LEF) families of transcription factors, leading to the transcription of Wnt target genes involved in tumor formation (Behrens et al., 1996; Huber et al., 1996; Korinek et al., 1997; Munemitsu et al., 1995). In the absence of a Wnt signal, APC, phosphorylated by glycogen synthase kinase 3β (GSK3β), binds to β-catenin and promotes its degradation, thereby preventing the transcription of Wnt target genes. In addition to the β-catenin-binding sites, the central region of APC also contains repeats of a Ser-Ala-Met-Pro (SAMP) motif, which binds to Axin or conductin, and appears to be essential for optimal regulation of Wnt signaling (Behrens et al., 1998; Hart et al., 1998; Kishida et al., 1998; Nakamura et al., 1998; Smits et al., 1999). Most of the tumor-associated mutations in the *apc* gene have been mapped within the central region (residues 1286–1513) (Miyaki et al., 1994; Miyoshi et al., 1992). Such *apc* mutations result in truncated APC proteins that lack all of the axin/conductin-binding SAMP motifs and some of the β-catenin-binding 20 amino acid repeats (Polakis, 1995).

The Arm domain in the N-terminal region of APC binds a variety of proteins (Figure 1A), suggesting that APC may also be involved in the regulation of cell-cell adhesion, cell polarization, and cell migration. The Arm-binding partners include the B56 regulatory subunit of protein phosphatase 2A (PP2A) (Seeling et al., 1999), APC-stimulated guanine nucleotide exchange factor (Asef) (Kawasaki et al., 2000), kinesin superfamily-associated protein 3

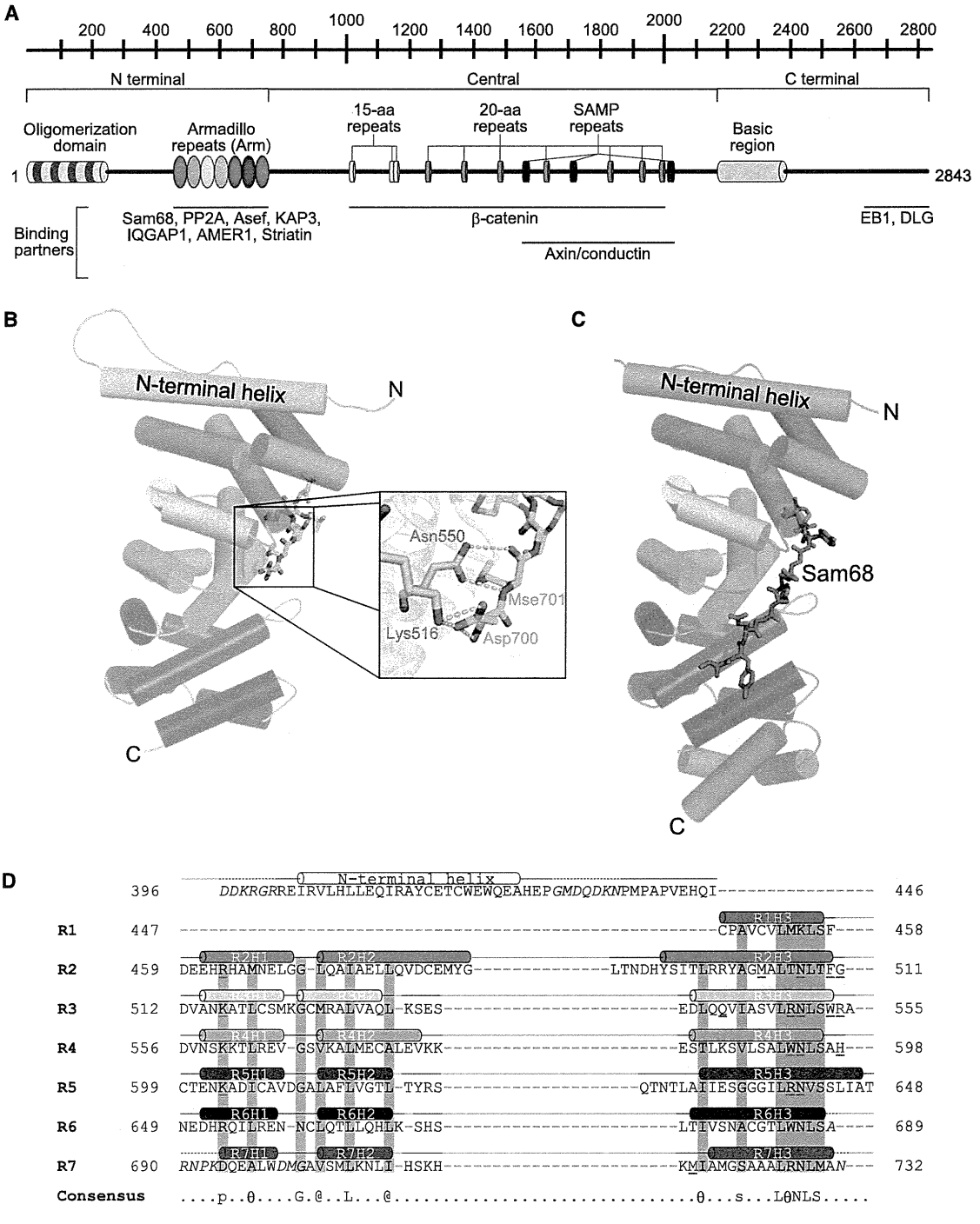

Figure 1. Overall Structure of APC-Arm

(A) Schematic representation of APC. The Arm domain is rainbow colored from the N terminus in red to the C terminus in violet. APC binds to several proteins, with the majority binding to the Arm domain or the central region.

(B) The overall structure of free APC-Arm. The H1, H2, and H3 helices of APC-Arm are rainbow colored. Residues 700–707, shown as a cyan stick representation, interact with the residues in the groove of the APC-Arm superhelix (close-up view). See Figure S1A for the electron density map of residues 700–707.

(C) The overall structure of the complex between APC-Arm and Sam68. The H1, H2, and H3 helices of APC-Arm are rainbow colored. Sam68, shown as a magenta stick representation, interacts with the residues in the groove of the APC-Arm superhelix. See Figure S1B for the electron density map of Sam68.

(D) Primary sequence and secondary structure of APC-Arm in the Sam68-bound structure. The H1, H2, and H3 helices of APC-Arm are rainbow colored. The repeats are aligned to show the sequence conservation (gray-shaded residues) among them. Disordered residues are italicized, and gaps are shown as hyphens. The residues that interact with Sam68 are underscored in magenta. On the line marked "Consensus," the single-letter code (uppercase letters) is listed if the residue is present in at least five repeats. Structural positions with a strong preference for a group of amino acids are listed on the line marked "Consensus," with the following symbols: p, polar (D, E, H, K, N, Q, R, S, T); θ, hydrophobic (A, C, F, H, I, L, M, T, V, W, Y); @, aliphatic (I, L, V); s, small (A, C, D, G, N, P, S, T, V).

(KAP3) (Jimbo et al., 2002), IQ-domain GTPase-activating protein 1 (IQGAP1) (Watanabe et al., 2004), APC membrane recruitment 1 (AMER1) (Grohmann et al., 2007), and Striatin (Breitman et al., 2008). We recently found that APC also binds to Sam68, the Src-associated in mitosis, 68 kDa protein, using a yeast two-hybrid system and an in vitro pull-down assay (unpublished data). Sam68 is a nuclear RNA-binding protein and may link the signaling pathways with the regulation of RNA metabolism (Lukong and Richard, 2003). The complex between APC and Sam68 regulates TCF-1 alternative splicing. However, mutations of APC that truncate regions downstream of the Arm domain of APC lead to the accumulation of the TCF-1E splice variant, which strongly transactivates Wnt target genes. Based on these data, we suggest that the control of Sam68-mediated pre-mRNA splicing might be another mechanism by which APC regulates Wnt signaling.

Despite the multitude of studies on the binding partners and functions of the Arm domain of APC, no structural information is available for this domain of APC. The lack of a three-dimensional structure has hindered our understanding of the molecular nature of the Arm domain of APC, and its functional interactions with different ligands. In this study, we determined the crystal structures of APC-Arm and its complex with the APC-binding tyrosine-rich domain of Sam68 (Sam68-YY; Figure 2A), which revealed the superhelical structure of APC-Arm and its specific interactions with Sam68-YY. We also report the effects of mutations and phosphorylation on the formation of the APC-Arm•Sam68-YY complex. The present results provide a basis for the different ligand specificities of the Arm domains of APC and other Arm-containing proteins.

RESULTS

Structure Determination

We have determined the structures of the APC-Arm fragment, consisting of residues 396–732, and its complex with the Sam68-YY fragment, consisting of residues 365–419. The structure of the free APC-Arm was determined by the MAD phasing method, with selenium as the anomalous scatterer, and refined at 2.1 Å resolution. The structure of the APC-Arm•Sam68-YY complex was determined by molecular replacement, using the APC-Arm structure as a search model, and refined at 2.4 Å resolution. The crystallographic data for APC-Arm and APC-Arm•Sam68-YY are summarized in Table 1.

Both crystals belong to the hexagonal space group $P6_1$ but have different unit-cell dimensions. The crystallographic asymmetric unit of the free APC-Arm contains only one molecule, whereas that of APC-Arm•Sam68-YY contains two complexes (see Figure S2A available online). The root-mean-square deviations (rmsds) of the Cα positions between the free and Sam68-bound forms of APC-Arm are 0.76 and 0.84 Å for complexes A and B, respectively. The following description of the APC-Arm•Sam68-YY complex refers only to complex B because the structures are nearly identical (rmsd of 0.55 Å for the comparable Cα positions; Figure S2B).

Structure of APC-Arm

In the free APC-Arm structure, only 8 residues (residues 700–707) among the last 43 residues were visible (Figure S1A). By contrast, in the Sam68-bound structure, most of the residues in the C-terminal region were visible, but residues 396–401 and 430–437 in the N-terminal region were disordered. Unless otherwise stated, only the APC-Arm molecule in the APC-Arm•Sam68-YY complex will be discussed hereafter in detail.

Based on its sequence, the APC region consisting of residues 452–767 was predicted to form seven Arm repeats (R1–R7) (Peifer et al., 1994; Hirschl et al., 1996). A sequence alignment among the APC proteins and homologs from different organisms revealed that the linker between the first two α helices in the APC-Arm structure (residues 427–446) is only weakly conserved, whereas all of the other regions in APC-Arm are highly conserved (Figure 3A). Thus, we will refer to the first α helix (residues 404–426) as the N-terminal helix, and the second α helix (residues 447–457) as the beginning of the Arm domain (Figure 1D).

The overall shape of APC-Arm is cylindrical, with an approximate length of 65 Å and diameter of 33 Å. The seven Arm repeats form a right-handed superhelix (Figure 1C). Each repeat is composed of three α helices, H1, H2, and H3, except that H1 and H2 are missing from R1. The Arm repeats R2–R7 are homologous, with the conserved residues among the repeats participating in similar intra- and inter-repeat interactions (Figure 1D). H3 has a highly conserved LθNLS sequence motif (where θ is a hydrophobic residue) near its C terminus. The two Leu residues participate in the intra-repeat interactions with the conserved residues in H1 and H2. The side chains of the hydrophobic, Asn, and Ser residues are located on the surface of the repeat, and mediate the inter-repeat interactions.

The groove of the APC-Arm superhelix is L-shaped and is large enough to accommodate a polypeptide chain (Figure 2B). The groove surface exhibits pronounced positive potentials, ascribed to the side chains of basic residues in H1 and H3. Similarly, other Arm domain-containing proteins, such as β-catenin (Daniels and Weis, 2002; Eklof Spink et al., 2001; Graham et al., 2000, 2001, 2002; Ha et al., 2004; Huber and Weis, 2001; Poy et al., 2001; Sampietro et al., 2006; Sun and Weis, 2011; Xing et al., 2004) and p120 catenin (p120; Ishiyama et al., 2010), have a positively charged groove that binds ligand peptides bearing an overall negative charge. Karyopherin α, on the other hand, has a negatively charged groove that binds positively charged NLS motifs (Conti et al., 1998).

In the Sam68-free APC-Arm structure, R7 is unfolded, and only residues 700–707 were visible, as described above. This eight residue region binds in an extended conformation to the positively charged groove (Figure 1B). Only two residues in this region, Asp700 and Mse701, interact with residues in the superhelix. In the Sam68-bound APC-Arm structure, there are several hydrogen bonds at the first five inter-repeat interfaces, but there is only one at the interface between R6 and R7. This weaker interaction between R6 and R7 could explain the propensity of R7 for unfolding, as seen in the free APC-Arm structure. Incidentally, we found that another APC-Arm fragment, lacking the entire R7 repeat, has a strong tendency to aggregate in solution (data not shown). This finding raises the possibility that the R7 repeat of APC-Arm enhances the stability of APC in the absence of the ligand peptide, by unfolding and shielding the peptide-binding site on APC-Arm.

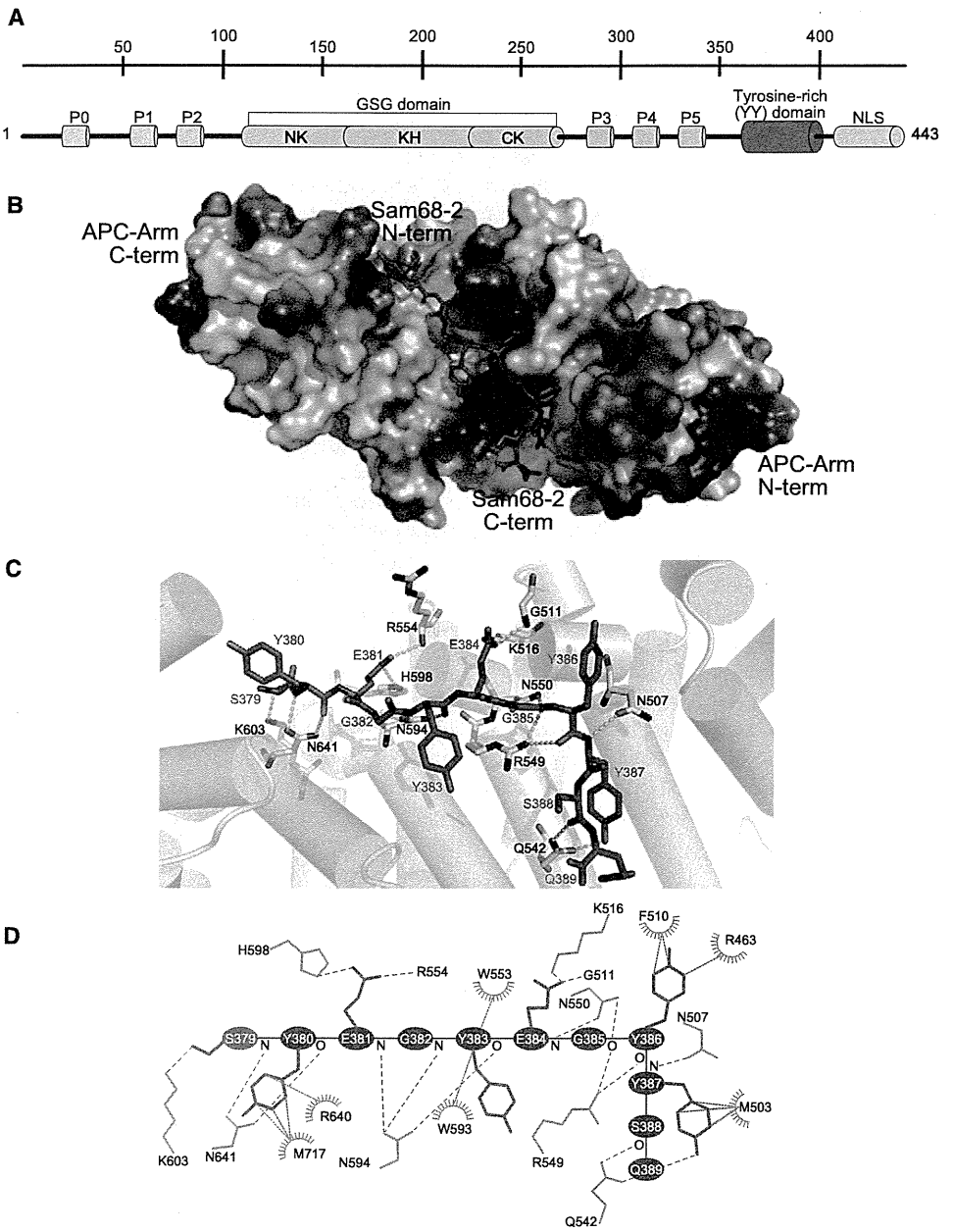

Figure 2. Sam68 Binds to the Positively Charged Groove of the APC-Arm Superhelix

(A) Schematic representation of Sam68. The YY domain of Sam68 is colored magenta.

(B) The Sam68-2 peptide (magenta; see Figure 3B for the location in Sam68-YY) atop the APC-Arm molecular surface. The positively and negatively charged regions are colored blue and red, respectively. Sam68-2 buries approximately 1740 Å^2 of the total solvent accessible area. There are two molecules of the APC-Arm•Sam68-2 complex, which are packed in a tail-to-tail manner (see Figure S2). C-term, C-terminal; N-term, N-terminal.

(C) Sam68-2 (magenta) and APC-Arm (gray) form extensive hydrogen bonds, which are shown as yellow dashed lines.

(D) The Sam68-2 bonding diagram. APC-Arm residues (gray) that form hydrophobic contacts with Sam68-2 (magenta) are denoted with a starburst. Hydrogen bonds and hydrophobic contacts are shown as yellow and gray dashed lines, respectively.

Interaction of APC-Arm with Sam68

We used the 55 residue fragment Sam68-YY for crystallization, but only residues 379–389 (Sam68-2) are visible in our electron density map (Figure S1B). Residues 379–386 form a roughly perpendicular extension, relative to the H3 helices of R3, R4, and R5 of APC-Arm (Figure 2B). On the other hand, residues 387–389 are bound in an antiparallel manner to the H3 helices of R2 and R3, and Sam68-2 is bent by approximately 90° at Tyr387. It is possible that Sam68-2 assumes a bent conformation to become fixed in the L-shaped groove of APC-Arm.

Sam68-2 is anchored in place by intermolecular hydrogen bonding and van der Waals interactions with the residues in APC-Arm repeats R2–R5 (Figures 2C and 2D). The side chains of Sam68-2 Ser379, Glu381, and Glu384 hydrogen bond with

Table 1. Crystallographic Data and Refinement Statistics

	APC-Arm			APC-Arm• Sam68-YY
Data Sets	Peak	Inflection	Remote	Native
Data Collection				
Beamline	SPring-8 BL26B1			SLS X06DA (PXIII)
Temperature (K)	100			100
Wavelength (Å)	0.97897	0.97934	0.96400	1.000
Resolution (Å)	50.0–2.12 (2.16–2.12)	50.0–2.10 (2.14–2.10)	50.0–2.14 (2.18–2.14)	64.0–2.40 (2.53–2.40)[a]
Space group	$P6_1$			$P6_1$
Cell dimensions				
a, *b*, *c* (Å)	114.30, 114.30, 61.80			148.22, 148.22, 63.38
α, β, γ (°)	90, 90, 120			90, 90, 120
Number of complexes in the asymmetric unit	1			2
Number of measured reflections	296,308 (13,493)	304,076 (12,652)	289,710 (12,676)	350,457 (49,116)
Number of unique reflections	26,244 (1,310)	27,064 (1,346)	25,630 (1,255)	31,344 (4,539)
Data completeness (%)	100 (100)	100 (100)	100 (100)	100 (100)
R_{merge}[b]	8.9 (49.9)	7.7 (62.3)	8.1 (54.4)	9.5 (38.8)
I/σ	24.6 (4.8)	29.5 (3.5)	29.5 (4.3)	7.1 (2.0)
Multiplicity	11.3 (10.3)	11.2 (9.4)	11.3 (10.1)	11.2 (10.8)
Refinement Statistics				
Number of reflections	27,029			29,744
Number of protein atoms	2,328			5116
Number of water molecules	117			264
R_{work}/R_{free} (%)[c]	20.4/23.2			18.7/23.0
Rmsd bond length (Å)	0.005			0.010
Rmsd bond angles (°)	0.9			1.1
Ramachandran plot				
Most favored regions (%)	95.6			96.4
Additional allowed regions (%)	4.4			3.6
Disallowed regions (%)	0			0

[a] The values in parentheses are for the highest resolution bin.
[b] $\sum_{hkl}\sum_i|I_i - \langle I \rangle|/|\langle I \rangle|$, where I_i is the intensity for the *i*th measurement of an equivalent reflection with indices *h*, *k*, *l*.
[c] $\sum||F_{obs}| - |F_{calc}||/\sum|F_{obs}|$, where the crystallographic R factor is calculated including and excluding refinement reflections. In each refinement, free reflections consist of 5% of the total number of reflections.

those of APC-Arm Lys603, His598, and Lys516, respectively. Most of the backbone oxygens and nitrogens of Sam68-2 hydrogen bond with the side chains of the highly conserved Asn residues in the LθNLS motifs of the H3 helices of APC-Arm. The aromatic rings of Sam68-2 Tyr380, Tyr386, and Tyr387 form hydrophobic interactions with the side chains of bulky residues in APC-Arm.

It is worth noting that Gln542 is the only residue in APC-Arm that forms both side chain to side chain and side chain to backbone interactions with Sam68-2. The side chain of APC-Arm Gln542 interacts with both the hydroxyl group of Sam68-2 Tyr387 and the backbone oxygen of Sam68-2 Ser388. These hydrogen bonds of APC-Arm Gln542 may be crucial for stabilizing the bent conformation of Sam68-2.

Thermodynamics of APC-Sam68 and APC-Asef Interactions

We used isothermal titration calorimetry (ITC) to precisely determine the thermodynamic-binding parameters (Figure 4). Sam68-YY binds to APC-Arm with a dissociation constant (K_D) of 161 nM (Figure 4G). The highly unfavorable entropy of binding of Sam68-YY to APC-Arm (Figure 4G) suggests that Sam68-YY is mostly unstructured in solution. Three regions in Sam68-YY (Sam68-1, Sam68-3, and Sam68-4) have sequences that are similar to that of the Sam68-2 peptide (Figure 3B). To examine if APC-Arm can bind to these three regions of Sam68-YY as well as Sam68-2, we performed ITC measurements on the four Sam68 peptides (Figure 4A; Figure S3). The Sam68-1, Sam68-3, and Sam68-4 peptides did not bind to APC-Arm. In contrast the Sam68-2 peptide showed affinity for APC-Arm in the single micromolar range (K_D = 7.3 μM; Figure 4G). However, the APC-Arm-binding affinity of Sam68-2 is lower than that of Sam68-YY. This could indicate that the residues flanking the N and C termini of Sam68-2 enhance the interaction of Sam68-YY with APC-Arm by binding, albeit weakly, to APC-Arm regions other than the positively charged groove, where Sam68-2 binds.

The Asef fragment consisting of residues 164–253, which contains both the APC-binding region (ABR) and SH3 domain (Asef-ABR-SH3), binds to APC-Arm 100-fold more strongly than Sam68-YY (Figures 4B and 4G; Figure S3). Moreover, the

thermodynamics of APC-Arm binding differ markedly between Sam68-YY and Asef-ABR-SH3. Sam68-YY binds to APC-Arm with a large, favorable binding enthalpy that is compensated by a large, unfavorable entropy. In contrast, Asef-ABR-SH3 binds to APC-Arm with a small binding enthalpy and a slightly favorable entropy term. This could reflect some intrinsic differences between Sam68-YY and Asef-ABR-SH3, such as flexibility, different modes of binding, or a combination of both.

We noticed that the sequence of residues 161–171 within human Asef-ABR (Kawasaki et al., 2000; Mitin et al., 2007) is somewhat homologous to that of Sam68-2. The residues corresponding to Sam68-2 Glu381, Tyr383, and Glu384 in this Asef sequence are Asp163, Tyr165, and Asp166. Despite the sequence similarity, the ITC-binding analysis revealed that the Asef fragment does not bind to APC-Arm (Figures 4B and 4G; Figure S3).

Mutational Analysis on APC-Arm and Sam68-YY

We also performed ITC measurements with APC-Arm and Sam68-YY mutants to confirm the importance of the residues on the binding interface of the APC-Arm•Sam68-YY complex (Figures 4C and 4D; Figure S3). The APC-Arm-K516E and -R549E mutants showed reduced binding affinity for Sam68-YY, as compared to the wild-type APC-Arm (the K_D values of the APC-Arm-K516E and -R549E mutants with Sam68-YY were 8.8 and 69 μM, respectively). On the other hand, the affinities of the APC-Arm-H598A and APC-Arm-K603E mutants (the K_D values of the APC-Arm-H598A and -K603E mutants with Sam68-YY were 498 and 606 nM, respectively) for Sam68-YY are close to that of the wild-type APC-Arm. The side chains of APC-Arm His598 and Sam68-2 Glu381 form a rather weak hydrogen bond (the distance between the NE2 atom of APC-Arm His598 and the OE2 atom of Sam68-2 Glu381 is 3.21 Å). Furthermore, a basic residue, Lys560, forms a water-mediated interaction with Sam68-2 Glu381. In the APC-Arm-H598A mutant, Lys560 may function to keep Sam68-YY in place, which explains the similar binding affinity of this mutant for Sam68-YY. In the case of the APC-Arm-K603E mutant, the side chain of Glu603, which is at the periphery of APC-Arm, may swing out toward the solvent region, thus avoiding a steric clash with the Sam68-YY Ser379 residue.

Next, we tested mutants of the Sam68-2 peptide against the wild-type APC-Arm (Figure 4D; Figure S3). The E381K and E384K mutations completely abolished the ability of Sam68-2 to bind to APC-Arm. Moreover, the Sam68-2-Y383A mutant showed significantly decreased affinity for APC-Arm, with a K_D value (88 μM) more than one order of magnitude higher than that of the wild-type Sam68-2. Interestingly, the Sam68-2-S379K mutant exhibited a K_D value of 18.5 μM, which is not much larger than that of the wild-type Sam68-2. The Ser379 residue is located at the N terminus of the Sam68-2 peptide and appears to have a more flexible side-chain conformation, as compared to the rest of the Sam68-2 residues. The side chain of Lys379 in the Sam68-2-S379K mutant may be directed out toward the solvent region, thus preventing a steric clash with the APC-Arm Lys603 residue.

Missense Mutations in APC-Arm

Based on data from the Human Gene Mutation Database (http://www.hgmd.cf.ac.uk/), there are several amino acid residues that are targets for missense mutations in the Arm domain of APC. One such target, Lys516, interacts with the Glu384 residue of Sam68 (Figure 5). In this study we found that the binding affinity of the APC-Arm-K516E mutant for Sam68-YY is lower than that of the wild-type APC-Arm. The K516N missense mutation was identified in a patient diagnosed with FAP (Cowie et al., 2004). Thus, we performed ITC measurements to directly test the effect of the K516N mutation on the binding of APC-Arm to its ligands. As expected, the APC-Arm-K516N mutant showed reduced binding affinity for Sam68-YY and Asef-ABR-SH3, by 21- and 9-fold, respectively (Figure 4E; Figure S3). Likewise, because Lys516 is located on the surface of the positively charged groove of APC-Arm, the APC-K516N mutant may have lower affinity, as compared to the wild-type APC-Arm, for the other APC-Arm-binding proteins.

Another target for a missense mutation, Arg414, is located on the surface of the Arm R1 repeat (Figure 5). The mutation of this residue could disrupt ligand binding, if that were its role. Moreover, Arg414 forms a hydrogen bond with the Leu469 residue in the neighboring R2 repeat. The R414C mutation found in patients with FAP (Nishisho et al., 1991) impairs this inter-repeat interaction. The two remaining targets for missense mutations in the Arm domain of APC, Ala501 (Wu et al., 2001) and Ser722 (Stella et al., 1994), would not directly affect ligand binding because these residues are buried (Figure 5). However, considering the rigidity of these residues and the residues surrounding them, it is likely that mutations at these positions would cause local structural distortion and/or destabilization of the Arm domain of APC, which may indirectly affect its function.

Effect of Tyrosine Phosphorylation on the Binding of Sam68-YY to APC-Arm

Sam68-YY has a cluster of 13 Tyr residues, which are potential sites of phosphorylation by several kinases, including Src (Fumagalli et al., 1994; Taylor and Shalloway, 1994) and Fyn (Richard et al., 1995). To assess whether phosphorylation affects Sam68-2 binding to APC-Arm, we performed ITC on four Sam68-2 peptides with phosphorylated Tyr (Sam68-2-pY380, -pY383, -pY386, and -pY387) (Figure 4F; Figure S3). The phosphorylation of Tyr387 completely abolished the APC-Arm binding. The presence of a phosphoryl group on Tyr387 in Sam68 may generate a steric clash with APC Gln542. To avoid this steric clash, Sam68-2 may adopt a completely elongated conformation, which could explain the inability of Sam68-2-pY387 to bind to APC-Arm. By contrast the phosphorylations of Tyr380, Tyr383, and Tyr386 did not drastically change their APC-Arm-binding abilities (the K_D values of the Sam68-2-pY380, -pY383, and -pY386 peptides with APC-Arm were 7.1, 25.9, and 3.2 μM, respectively).

DISCUSSION

The Arm domain is highly conserved in APC proteins and their homologs (Figure 3A), and provides a binding site for various proteins involved in Wnt signaling and other cellular processes. Here, we report two crystal structures of APC-Arm, in an effort to clarify the molecular nature of the interactions between APC-Arm and Sam68. In the complex structure the Sam68-2

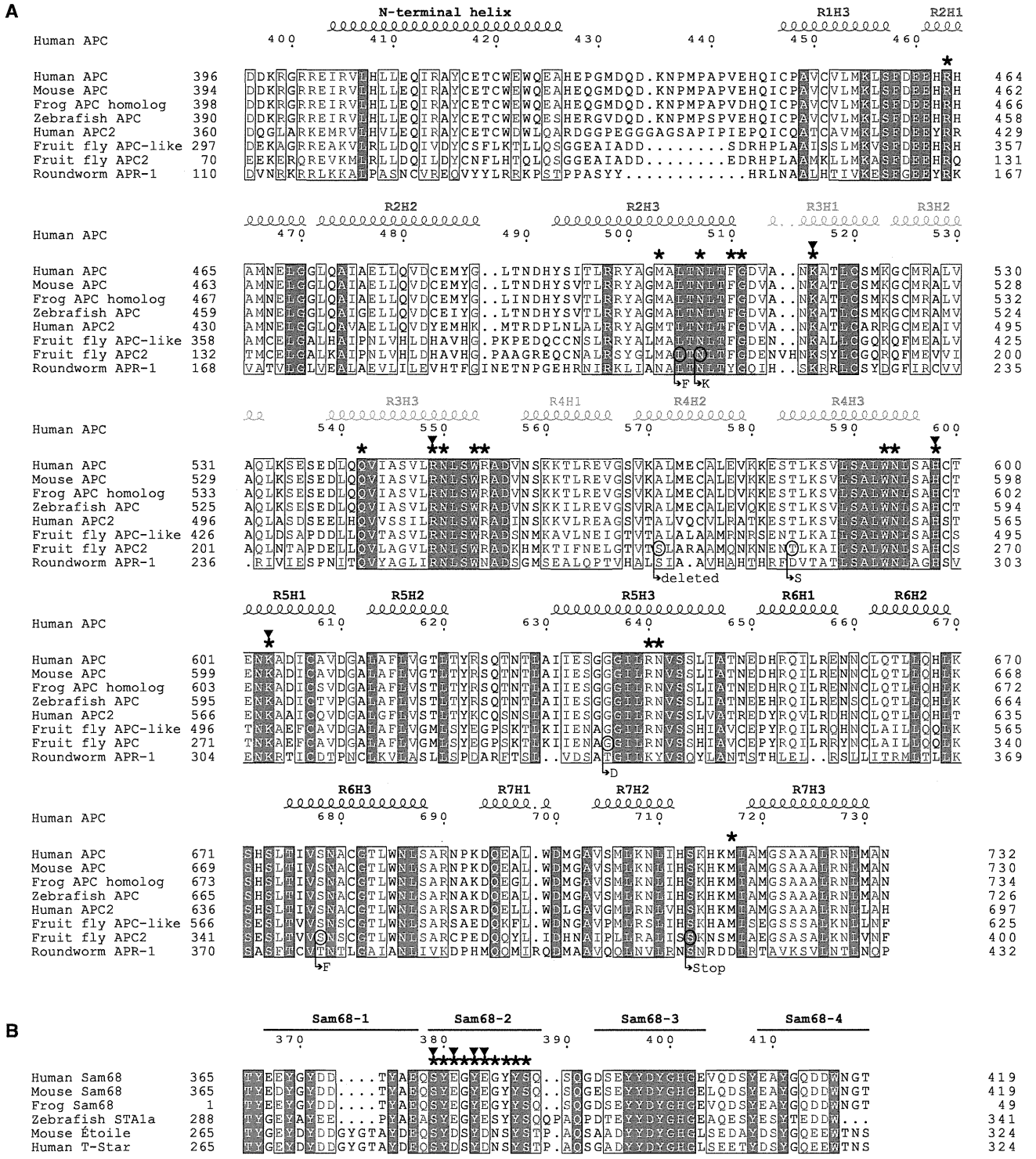

Figure 3. Sequence Alignment of the APC Proteins and Homologs, and of the Sam68 Proteins and Homologs

(A) Sequence alignment of the Arm domains of APC proteins and homologs from different organisms. The secondary structures of human APC-Arm complexed with Sam68-2 are shown above the sequences. Asterisks indicate the contact residues of APC with Sam68 in the APC-Arm • Sam68-YY complex. The positions of the APC-Arm residues that were mutated in Figure 4C are indicated with arrowheads. The residues that are mutated in fruit fly APC2 are encircled (McCartney et al., 1999, 2006). Primary sequences used in the alignment: human APC (accession number AAA03586); mouse APC (NP_031488); frog APC homolog (NP_001084351); zebrafish APC (NP_001137312); human APC2 (AAH32573); fruit fly APC-like protein (NP_477152); fruit fly APC2 (NP_477430); and roundworm APC-related protein 1 (APR-1; AAC47747). In human APC-Arm, the H3 helices define the binding groove for Sam68. By analogy to the human APC-Arm structure, five of the seven residues that are targeted for missense mutations in the fruit fly APC2 fall within the H3 helices. Thus, the fruit fly APC2 mutations in the H3 helices may affect ligand binding to APC2.

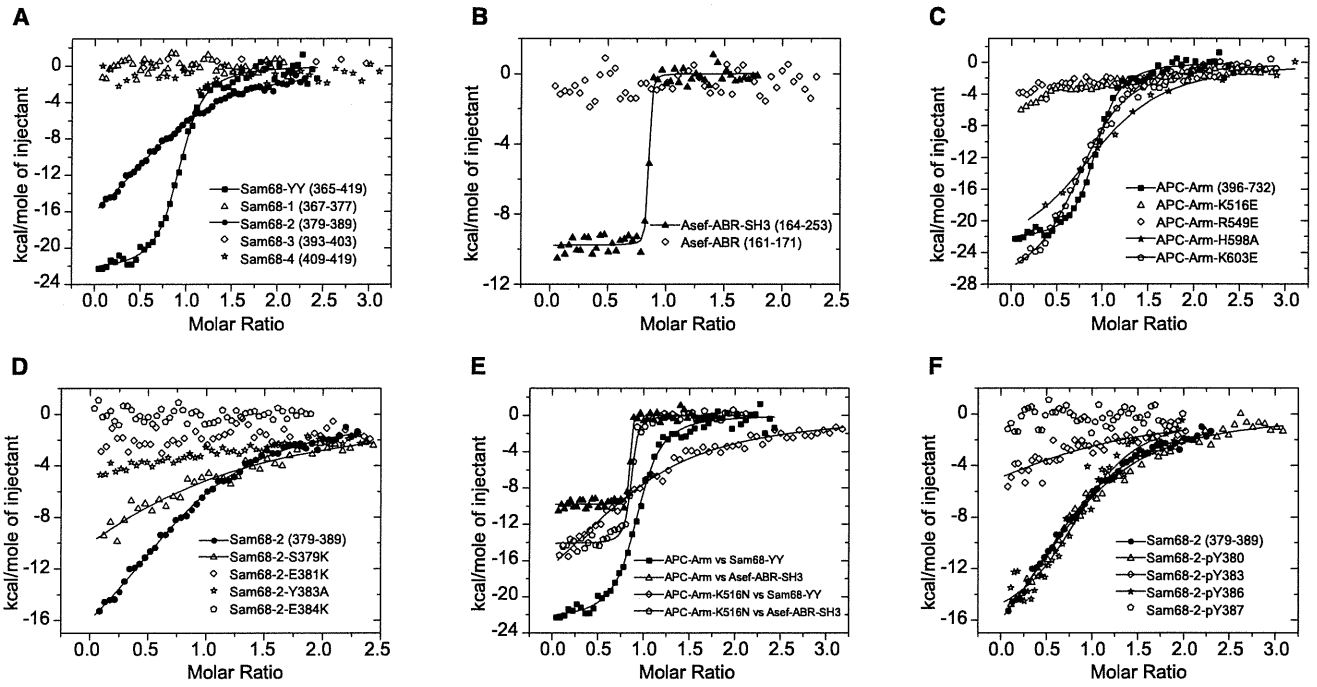

G

Cell	Syringe	*N*	K_D (nM)	ΔH (kcal mol^{-1})	TΔS (kcal mol^{-1})	ΔG (kcal mol^{-1})
APC-Arm	Sam68-YY	0.93 ± 0.01	161 ± 17	-22.5 ± 0.2	-13.1	-9.4
APC-Arm	Sam68-2	0.83 ± 0.02	7300 ± 500	-22.4 ± 0.7	-15.5	-6.9
APC-Arm	Asef-ABR-SH3	0.84 ± 0.00	1.60 ± 1.43	-9.8 ± 0.1	2.2	-12.0

Figure 4. ITC Analysis of the Interaction between APC-Arm and Sam68

(A) Sam68-YY binds to APC-Arm, with a K_D of 161 nM. ITC experiments demonstrated that among the four peptides in (A), only Sam68-2 (closed circles) binds to APC-Arm, but its interaction is weaker, as compared to that of Sam68-YY (K_D = 7.3 μM).

(B) Asef-ABR-SH3 binds to APC-Arm, with a K_D of 1.6 nM, but the Asef-ABR fragment, whose sequence is similar to that of Sam68-2 (residues 161–171), does not bind to APC-Arm.

(C) Binding contributions of the APC-Arm Lys516, Arg549, His598, and Lys603 residues were assessed by mutagenesis and ITC. Wild-type APC-Arm binding to Sam68-YY (closed squares) is shown for comparison.

(D) Analysis of the binding contributions of the Sam68-2 Ser379, Glu381, Tyr383, and Glu384 residues by mutagenesis and ITC. Wild-type Sam68-2 binding to APC-Arm (closed circles) is shown for comparison.

(E) The effects of the K516N missense mutation found in a patient with FAP (see Figure 5) on the binding of APC-Arm to Sam68-YY and Asef-ABR-SH3 were analyzed by mutagenesis and ITC. Wild-type Sam68-YY and Asef-ABR-SH3 binding to APC-Arm (closed squares and triangles, respectively) is shown for comparison.

(F) Phosphorylations of the Tyr residues in Sam68-2 exert minimal effects on binding to APC-Arm, except for that of Tyr387 (open pentagons). Nonphosphorylated Sam68-2 is shown for comparison (closed circles). See Figure S3.

(G) Tabulation of energetic parameters for the binding of Sam68 or Asef to APC-Arm, from ITC-binding curves. *N* is the stoichiometry, and T is the absolute temperature (298 K). ΔH, ΔS, and ΔG are the changes in binding enthalpy, entropy, and Gibbs energy, respectively.

peptide adopts a bent conformation upon binding to the L-shaped groove of APC-Arm. Our mutational analysis showed that the strictly conserved APC Arg549 and Lys516 residues (Figure 3A), as well as the highly conserved Sam68 Glu381, Tyr383, and Glu384 residues (Figure 3B), are particularly important for the formation of the APC-Arm•Sam68-YY complex.

We found that β-catenin does not bind to Sam68 in vitro (unpublished data). There are no known overlapping binding

(B) Sequence alignment of the YY domains of Sam68 proteins and homologs from different organisms. The location of Sam68-2, as seen in the crystal structure, and those of the regions with sequences similar to Sam68-2 (Sam68-1, -3, and -4) are shown above the sequences. Asterisks indicate the contact residues of Sam68 with APC in the APC-Arm•Sam68-YY complex. The positions of the Sam68-2 residues that were mutated in Figure 4D are indicated with arrowheads. Primary sequences used in the alignment: human Sam68 (Q07666); mouse Sam68 (AAA86693); frog Sam68 (AAP82291); zebrafish signal transducer and transcriptional activator protein 1a (STA1a; NP_571000); mouse Sam68-like protein 2 (Étoile; NP_034288); and human Sam68-like protein 2 (T-Star; NP_006549). This figure was generated by ESPript (Gouet et al., 1999).

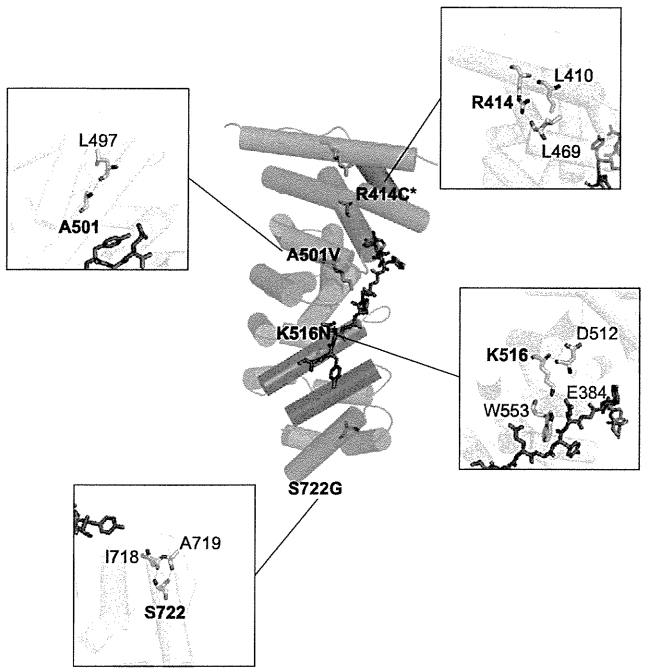

Figure 5. Locations of Missense Mutations in APC-Arm
The amino acid residues that are targets for missense mutations are indicated in bold letters. Mutations of APC-Arm surface residues (marked with an asterisk) are likely to affect ligand binding. The mutation of the Lys516 residue of APC-Arm, which interacts with Glu384 of Sam68 (magenta), to an Asn residue lowers the binding affinity of APC-Arm for Sam68-YY (see Figure 4E). Hydrogen bonds are shown as yellow dashed lines. The H1 and H2 helices of APC-Arm are colored gray, and the H3 helices are rainbow colored.

partners between the Arm domains of APC and β-catenin. Because both APC and β-catenin utilize their Arm domains to bind their respective ligand peptides, the question arises as to how two closely related proteins, existing in the same subcellular compartments, recognize different proteins. To answer this question, we compared the present APC-Arm structure to that of β-catenin-Arm. APC-Arm superimposes well onto β-catenin-Arm (Graham et al., 2000), with an rmsd of 1.62 Å for 209 Cα atoms (Figure 6A). However, we noted that the modes of ligand recognition between these proteins differ significantly. Only 5 of the 18 residues that interact with Sam68 residues in APC-Arm have identical residues at the corresponding positions in β-catenin-Arm (Figures 6C and 6E). Similarly, only 4 of the 15 residues that interact with the TCF3 residues in β-catenin-Arm (Graham et al., 2000) have identical residues at the corresponding positions in APC-Arm (Figure 6F). These differences support the distinct ligand specificities of the Arm domains of APC and β-catenin.

The overall structure of APC-Arm is similar to those of other Arm-containing proteins, such as p120 (Figure 6B), plakophilin 1, plakoglobin, and karyopherin α (Figure S4). Of the 18 residues that interact with Sam68 residues in APC-Arm, 8 have identical residues at the corresponding positions in p120-Arm (Figures 6D and 6E). Moreover, 8 of the 20 residues that interact with residues in the juxtamembrane domain of E-cadherin (Ecad-JMD) in p120-Arm have identical residues at the corresponding positions in APC-Arm (Figure 6G). However, Ecad-JMD in the p120-Arm•Ecad-JMD complex structure is extended, whereas Sam68-2 adopts a bent conformation in the APC-Arm•Sam68-2 complex structure (Figure 6D). In Ecad-JMD the Tyr387 residue, at the apex of the Sam68-2 bend, is replaced by a Phe residue. In p120-Arm the APC-Arm Gln542 residue, which interacts with Sam68-2 Tyr387, is replaced by a Thr residue. It would be interesting to determine whether APC-Arm and p120-Arm have overlapping binding partners and, if not, whether these differences support the lack of common partners.

It has been suggested that the function of Sam68 in alternative splicing is regulated by phosphorylation (Paronetto et al., 2007). In the present study, we determined the effect of phosphorylation of the Tyr residues in Sam68-2 on APC-Arm binding. We showed that the phosphorylation of three of the four Tyr residues in Sam68-2 had little effect on binding to APC-Arm. However, the phosphorylation of the Tyr387 residue abrogated APC-Arm•Sam68-2 complex formation. Future studies will be necessary to identify the precise phosphorylation sites in Sam68-YY and to determine how phosphorylation affects Sam68-mediated TCF-1 alternative splicing.

EXPERIMENTAL PROCEDURES

Protein Expression and Purification

Selenomethionine (SeMet)-labeled and native human APC-Arm, native human Sam68-YY, and native Asef-ABR-SH3 were individually expressed in the cell-free expression system (Kigawa et al., 1999, 2004; Yabuki et al., 2007). The proteins were purified separately on a HisTrap column (GE Healthcare Bio-Sciences), eluted with imidazole, cleaved with TEV protease, and further purified by anion-exchange (HiTrap Q; GE Healthcare Bio-Sciences) and gel filtration chromatography (HiLoad 16/60 Superdex 75; GE Healthcare Bio-Sciences). Sam68-YY and Asef-ABR-SH3 were reloaded onto the HisTrap column after TEV cleavage. Native APC-Arm was mixed with an equimolar concentration of Sam68-YY prior to crystallization trials. See the Supplemental Experimental Procedures for more details.

Crystallization and Structure Determination

Selenomethionyl APC-Arm crystals were grown by mixing 1 μl of a 5 mg/ml protein preparation with 0.5 μl of reservoir solution, containing 0.1 M sodium acetate (pH 4.6) and 1.25 M lithium citrate, and equilibrating the mixture against 70 μl of the reservoir solution. Crystals of the APC-Arm•Sam68-YY complex were grown by the sitting-drop vapor diffusion method, by mixing 0.8 μl of a 5 mg/ml protein complex solution with 0.5 μl of reservoir solution, containing 0.1 M Bis-Tris (pH 5.5), 0.15 M NaCl, and 20% polyethylene glycol (PEG) 3350, and equilibrating the mixture against 70 μl of the reservoir solution. The crystals grew at 20°C after 2–3 days and reached a suitable size in 10–14 days. The crystals were cryoprotected in the reservoir solution supplemented with 15%–25% glycerol and flash cooled in liquid nitrogen. A MAD data set for the selenomethionyl APC-Arm crystal was collected at the RIKEN Structural Genomics Beamline I (BL26B1) at SPring-8. The data were processed with the HKL2000 program package (Otwinowski and Minor, 1997). The native data set for the APC-Arm•Sam68-YY crystal was collected at the X06DA (PXIII) Beamline at the Swiss Light Source. Data were processed using MOSFLM (Leslie, 1995) and scaled with SCALA (Collaborative Computational Project, Number 4, 1994).

The structure of the selenomethionine derivative of APC-Arm was solved by the MAD method with the programs SOLVE (Terwilliger and Berendzen, 1999) and RESOLVE (Terwilliger, 2000). The APC-Arm•Sam68-YY complex structure was solved by molecular replacement, using the structure of APC-Arm as a search model, with the program Phaser (McCoy et al., 2007). Successive rounds of manual model building and refinement were performed to refine the initial models. Refinement statistics are summarized in Table 1. See the Supplemental Experimental Procedures for more details.

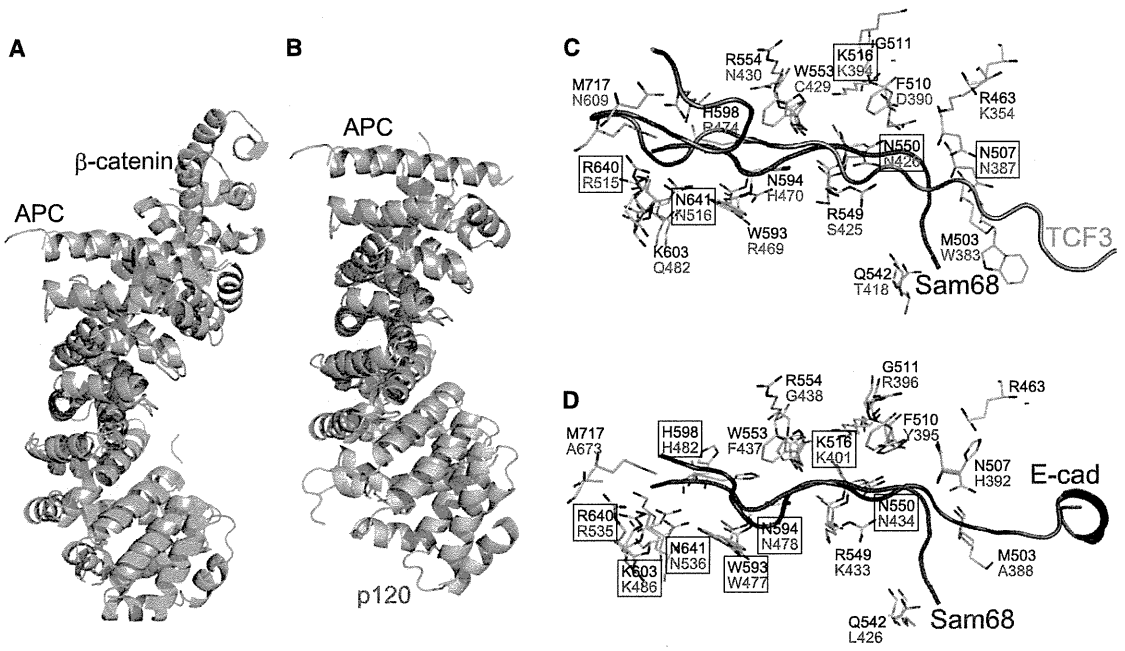

E

APC	β-cat	p120
R463	K354	-
M503	W383	A388
N507	N387	H392
F510	D390	Y395
G511	-	R396
◎ K516	K394	K401
Q542	T418	L426
◎ R549	S425	K433
N550	N426	N434
W553	C429	F437
R554	N430	G438
W593	R469	W477
N594	H470	N478
H598	R474	H482
K603	Q482	K486
R640	R515	R535
N641	N516	N536
M717	N609	A673

F

β-cat	APC	p120
Y306	-	F437
G307	-	G438
◎ K312	-	K444
R386	T506	R535
N387	N507	N536
D390	F510	S539
N426	N550	N585
C429	W553	Y588
◎ K435	K560	-
R469	W593	A687
H470	N594	G688
S473	A597	T691
R474	H598	Y692
K508	E633	K722
N516	N641	N730

G

p120	APC	β-cat
P366	-	G235
V371	I475	L240
M374	L478	M243
V382	L497	V251
N385	Y500	Y254
A386	A501	A255
Y389	A504	T258
Q391	T506	H260
H392	N507	N261
◎ K401	K516	K270
K433	R549	N302
N434	N550	I303
F437	W553	Y306
G438	R554	G307
K444	K560	K312
W477	W593	K345
◎ N478	N594	V346
K486	K603	K354
N536	N641	N387
K574	T675	D413

Figure 6. Conservation of the Sam68-Binding Residues in APC, β-Catenin, and p120

(A) Superposition of the Arm domains of APC (gray) and β-catenin (PDB accession 1G3J; green).

(B) Superposition of the Arm domains of APC (gray) and p120 (PDB accession 3L6X; yellow). See Figure S4 for superposition of the Arm domains of APC and other Arm-containing proteins.

(C) The Sam68-binding residues in APC (gray) are weakly conserved in β-catenin (green). Boxed residues are identical.

(D) Conservation of the Sam68-binding residues in APC (gray) and p120 (yellow). Boxed residues are identical.

(E) Conservation of the APC Sam68-binding residues in β-catenin and p120. The Sam68-binding residues in APC are listed in the left column. The APC residues that are important for APC-Arm • Sam68-YY complex formation, as validated by mutagenesis in this study, are marked with the symbol ◎ The β-catenin and p120 residues at the corresponding positions are listed in the middle and right columns, respectively. The β-catenin and p120 residues that are identical to the

ITC Measurements

All 11 amino acid peptides used for the ITC experiments were purchased from the Brain Science Institute at RIKEN. Samples were buffered with 20 mM Tris-HCl (pH 8.0) and 300 mM NaCl, centrifuged, and degassed prior to use. The ITC measurements were performed at 25°C with a MicroCal VP-ITC calorimeter. Aliquots of 100–250 μM titrant were stepwise injected into a 10–25 μM titrate. The data were analyzed with the MicroCal Origin software, using a binding model that assumes a single site of interaction (Wiseman et al., 1989). See the Supplemental Experimental Procedures for more details.

ACCESSION NUMBERS

Atomic coordinates and structure factors for the structures reported in this work have been deposited in the PDB, under the ID codes 3AU3 and 3QHE.

SUPPLEMENTAL INFORMATION

Supplemental Information includes four figures and Supplemental Experimental Procedures and can be found with this article online at doi:10.1016/j.str.2011.07.013.

ACKNOWLEDGMENTS

We thank R. Akasaka, M. Aoki, K. Honda, M. Inoue, T. Itagaki, K. Katsura, N. Maoka, N. Ohsawa, H. Shimizu, N. Shinya, M. Toyama, and T. Uchikubo-Kamo for help with sample preparation; T. Hosaka for X-ray diffraction data collection; T. Kasai and N. Tochio for technical assistance during ITC measurements; L.J. Parker for advice on data processing and structure determination, and for critical reading of the manuscript; and A. Shimada for assistance during ITC measurements and for helpful discussions. We thank the Support Unit for Bio-material Analysis, RIKEN BSI Research Resources Center, especially A. Abe, J. Ishikawa, and R. Ito, for synthesis of the Sam68 peptides; and the SPring-8 and SLS staffs for support. This work was supported by the RIKEN Structural Genomics/Proteomics Initiative (RSGI), the National Project on Protein Structural and Functional Analyses, and the Targeted Proteins Research Program (TPRP) from the Ministry of Education, Culture, Sports, Science and Technology (MEXT) of Japan.

Received: February 17, 2011
Revised: May 31, 2011
Accepted: July 4, 2011
Published: October 11, 2011

REFERENCES

Ashton-Rickardt, P.G., Dunlop, M.G., Nakamura, Y., Morris, R.G., Purdie, C.A., Steel, C.M., Evans, H.J., Bird, C.C., and Wyllie, A.H. (1989). High frequency of APC loss in sporadic colorectal carcinoma due to breaks clustered in 5q21-22. Oncogene *4*, 1169–1174.

Behrens, J., von Kries, J.P., Kühl, M., Bruhn, L., Wedlich, D., Grosschedl, R., and Birchmeier, W. (1996). Functional interaction of β-catenin with the transcription factor LEF-1. Nature *382*, 638–642.

Behrens, J., Jerchow, B.A., Würtele, M., Grimm, J., Asbrand, C., Wirtz, R., Kühl, M., Wedlich, D., and Birchmeier, W. (1998). Functional interaction of an axin homolog, conductin, with β-catenin, APC, and GSK3β. Science *280*, 596–599.

Bodmer, W.F., Bailey, C.J., Bodmer, J., Bussey, H.J., Ellis, A., Gorman, P., Lucibello, F.C., Murday, V.A., Rider, S.H., Scambler, P., et al. (1987). Localization of the gene for familial adenomatous polyposis on chromosome 5. Nature *328*, 614–616.

Breitman, M., Zilberberg, A., Caspi, M., and Rosin-Arbesfeld, R. (2008). The armadillo repeat domain of the APC tumor suppressor protein interacts with Striatin family members. Biochim. Biophys. Acta *1783*, 1792–1802.

Collaborative Computational Project, Number 4. (1994). The CCP4 suite: programs for protein crystallography. Acta Crystallogr. D Biol. Crystallogr. *50*, 760–763.

Conti, E., Uy, M., Leighton, L., Blobel, G., and Kuriyan, J. (1998). Crystallographic analysis of the recognition of a nuclear localization signal by the nuclear import factor karyopherin α. Cell *94*, 193–204.

Cowie, S., Drmanac, S., Swanson, D., Delgrosso, K., Huang, S., du Sart, D., Drmanac, R., Surrey, S., and Fortina, P. (2004). Identification of *APC* gene mutations in colorectal cancer using universal microarray-based combinatorial sequencing-by-hybridization. Hum. Mutat. *24*, 261–271.

Daniels, D.L., and Weis, W.I. (2002). ICAT inhibits β-catenin binding to Tcf/Lef-family transcription factors and the general coactivator p300 using independent structural modules. Mol. Cell *10*, 573–584.

Eklof Spink, K., Fridman, S.G., and Weis, W.I. (2001). Molecular mechanisms of β-catenin recognition by adenomatous polyposis coli revealed by the structure of an APC-β-catenin complex. EMBO J. *20*, 6203–6212.

Fodde, R., Edelmann, W., Yang, K., van Leeuwen, C., Carlson, C., Renault, B., Breukel, C., Alt, E., Lipkin, M., Khan, P.M., et al. (1994). A targeted chain-termination mutation in the mouse *Apc* gene results in multiple intestinal tumors. Proc. Natl. Acad. Sci. USA *91*, 8969–8973.

Fumagalli, S., Totty, N.F., Hsuan, J.J., and Courtneidge, S.A. (1994). A target for Src in mitosis. Nature *368*, 871–874.

Gouet, P., Courcelle, E., Stuart, D.I., and Métoz, F. (1999). ESPript: analysis of multiple sequence alignments in PostScript. Bioinformatics *15*, 305–308.

Graham, T.A., Weaver, C., Mao, F., Kimelman, D., and Xu, W. (2000). Crystal structure of a β-catenin/Tcf complex. Cell *103*, 885–896.

Graham, T.A., Ferkey, D.M., Mao, F., Kimelman, D., and Xu, W. (2001). Tcf4 can specifically recognize β-catenin using alternative conformations. Nat. Struct. Biol. *8*, 1048–1052.

Graham, T.A., Clements, W.K., Kimelman, D., and Xu, W. (2002). The crystal structure of the β-catenin/ICAT complex reveals the inhibitory mechanism of ICAT. Mol. Cell *10*, 563–571.

Groden, J., Thliveris, A., Samowitz, W., Carlson, M., Gelbert, L., Albertsen, H., Joslyn, G., Stevens, J., Spirio, L., Robertson, M., et al. (1991). Identification and characterization of the familial adenomatous polyposis coli gene. Cell *66*, 589–600.

Grohmann, A., Tanneberger, K., Alzner, A., Schneikert, J., and Behrens, J. (2007). AMER1 regulates the distribution of the tumor suppressor APC between microtubules and the plasma membrane. J. Cell Sci. *120*, 3738–3747.

Sam68-binding residues in APC are enclosed in green and yellow boxes, respectively. Both APC residues that are important for APC-Arm•Sam68-YY complex formation are conserved in p120, but not in β-catenin. The residue in p120 corresponding to APC Arg549 is a Lys residue and, thus, retains the positive charge.
(F) Conservation of the β-catenin TCF3-binding residues in APC and p120. The TCF3-binding residues in β-catenin are listed in the left column. The β-catenin residues that are important for β-catenin-Arm•TCF3 complex formation, as validated by mutagenesis (Graham et al., 2000), are marked with the symbol ◎ The APC and p120 residues at the corresponding positions are listed in the middle and right columns, respectively. The APC and p120 residues that are identical to the TCF3-binding residues in β-catenin are in enclosed in gray and yellow boxes, respectively. β-Catenin Lys312 is conserved in p120, but not in APC. On the other hand, β-catenin Lys435 is conserved in APC, but not in p120.
(G) Conservation of the p120 E-cad-binding residues in APC and β-catenin. The E-cad-binding residues in p120 are listed in the left column. The p120 residues that are important for p120-Arm•E-cad complex formation, as validated by mutagenesis (Ishiyama et al., 2010), are marked with the symbol ◎ The APC and β-catenin residues at the corresponding positions are listed in the middle and right columns, respectively. The APC and β-catenin residues that are identical to the E-cad binding residues in p120 are enclosed in gray and green boxes, respectively. Both p120 residues that are essential for the interaction with E-cad are conserved in APC, but not in β-catenin.

Ha, N.C., Tonozuka, T., Stamos, J.L., Choi, H.J., and Weis, W.I. (2004). Mechanism of phosphorylation-dependent binding of APC to β-catenin and its role in β-catenin degradation. Mol. Cell *15*, 511–521.

Hart, M.J., de los Santos, R., Albert, I.N., Rubinfeld, B., and Polakis, P. (1998). Downregulation of β-catenin by human Axin and its association with the APC tumor suppressor, β-catenin and GSK3 β. Curr. Biol. *8*, 573–581.

Hirschl, D., Bayer, P., and Müller, O. (1996). Secondary structure of an armadillo single repeat from the APC protein. FEBS Lett. *383*, 31–36.

Huber, A.H., and Weis, W.I. (2001). The structure of the β-catenin/E-cadherin complex and the molecular basis of diverse ligand recognition by β-catenin. Cell *105*, 391–402.

Huber, O., Korn, R., McLaughlin, J., Ohsugi, M., Herrmann, B.G., and Kemler, R. (1996). Nuclear localization of β-catenin by interaction with transcription factor LEF-1. Mech. Dev. *59*, 3–10.

Ishiyama, N., Lee, S.H., Liu, S., Li, G.Y., Smith, M.J., Reichardt, L.F., and Ikura, M. (2010). Dynamic and static interactions between p120 catenin and E-cadherin regulate the stability of cell-cell adhesion. Cell *141*, 117–128.

Itoh, K., Krupnik, V.E., and Sokol, S.Y. (1998). Axis determination in *Xenopus* involves biochemical interactions of axin, glycogen synthase kinase 3 and β-catenin. Curr. Biol. *8*, 591–594.

Jimbo, T., Kawasaki, Y., Koyama, R., Sato, R., Takada, S., Haraguchi, K., and Akiyama, T. (2002). Identification of a link between the tumour suppressor APC and the kinesin superfamily. Nat. Cell Biol. *4*, 323–327.

Kawasaki, Y., Senda, T., Ishidate, T., Koyama, R., Morishita, T., Iwayama, Y., Higuchi, O., and Akiyama, T. (2000). Asef, a link between the tumor suppressor APC and G-protein signaling. Science *289*, 1194–1197.

Kigawa, T., Yabuki, T., Yoshida, Y., Tsutsui, M., Ito, Y., Shibata, T., and Yokoyama, S. (1999). Cell-free production and stable-isotope labeling of milligram quantities of proteins. FEBS Lett. *442*, 15–19.

Kigawa, T., Yabuki, T., Matsuda, N., Matsuda, T., Nakajima, R., Tanaka, A., and Yokoyama, S. (2004). Preparation of *Escherichia coli* cell extract for highly productive cell-free protein expression. J. Struct. Funct. Genomics *5*, 63–68.

Kishida, S., Yamamoto, H., Ikeda, S., Kishida, M., Sakamoto, I., Koyama, S., and Kikuchi, A. (1998). Axin, a negative regulator of the wnt signaling pathway, directly interacts with adenomatous polyposis coli and regulates the stabilization of β-catenin. J. Biol. Chem. *273*, 10823–10826.

Korinek, V., Barker, N., Morin, P.J., van Wichen, D., de Weger, R., Kinzler, K.W., Vogelstein, B., and Clevers, H. (1997). Constitutive transcriptional activation by a β-catenin-Tcf complex in APC-/- colon carcinoma. Science *275*, 1784–1787.

Leppert, M., Dobbs, M., Scambler, P., O'Connell, P., Nakamura, Y., Stauffer, D., Woodward, S., Burt, R., Hughes, J., Gardner, E., et al. (1987). The gene for familial polyposis coli maps to the long arm of chromosome 5. Science *238*, 1411–1413.

Leslie, A.G.W. (1995). MOSFLM Users Guide (Cambridge: MRC Laboratory of Molecular Biology).

Lukong, K.E., and Richard, S. (2003). Sam68, the KH domain-containing superSTAR. Biochim. Biophys. Acta *1653*, 73–86.

McCartney, B.M., Dierick, H.A., Kirkpatrick, C., Moline, M.M., Baas, A., Peifer, M., and Bejsovec, A. (1999). *Drosophila* APC2 is a cytoskeletally-associated protein that regulates wingless signaling in the embryonic epidermis. J. Cell Biol. *146*, 1303–1318.

McCartney, B.M., Price, M.H., Webb, R.L., Hayden, M.A., Holot, L.M., Zhou, M., Bejsovec, A., and Peifer, M. (2006). Testing hypotheses for the functions of APC family proteins using null and truncation alleles in *Drosophila*. Development *133*, 2407–2418.

McCoy, A.J., Grosse-Kunstleve, R.W., Adams, P.D., Winn, M.D., Storoni, L.C., and Read, R.J. (2007). Phaser crystallographic software. J. Appl. Crystallogr. *40*, 658–674.

Mitin, N., Betts, L., Yohe, M.E., Der, C.J., Sondek, J., and Rossman, K.L. (2007). Release of autoinhibition of ASEF by APC leads to CDC42 activation and tumor suppression. Nat. Struct. Mol. Biol. *14*, 814–823.

Miyaki, M., Konishi, M., Kikuchi-Yanoshita, R., Enomoto, M., Igari, T., Tanaka, K., Muraoka, M., Takahashi, H., Amada, Y., Fukayama, M., et al. (1994). Characteristics of somatic mutation of the adenomatous polyposis coli gene in colorectal tumors. Cancer Res. *54*, 3011–3020.

Miyoshi, Y., Nagase, H., Ando, H., Horii, A., Ichii, S., Nakatsuru, S., Aoki, T., Miki, Y., Mori, T., and Nakamura, Y. (1992). Somatic mutations of the APC gene in colorectal tumors: mutation cluster region in the APC gene. Hum. Mol. Genet. *1*, 229–233.

Munemitsu, S., Albert, I., Souza, B., Rubinfeld, B., and Polakis, P. (1995). Regulation of intracellular β-catenin levels by the adenomatous polyposis coli (APC) tumor-suppressor protein. Proc. Natl. Acad. Sci. USA *92*, 3046–3050.

Nakamura, T., Hamada, F., Ishidate, T., Anai, K., Kawahara, K., Toyoshima, K., and Akiyama, T. (1998). Axin, an inhibitor of the Wnt signalling pathway, interacts with β-catenin, GSK-3β and APC and reduces the β-catenin level. Genes Cells *3*, 395–403.

Nishisho, I., Nakamura, Y., Miyoshi, Y., Miki, Y., Ando, H., Horii, A., Koyama, K., Utsunomiya, J., Baba, S., and Hedge, P. (1991). Mutations of chromosome 5q21 genes in FAP and colorectal cancer patients. Science *253*, 665–669.

Oshima, M., Oshima, H., Kitagawa, K., Kobayashi, M., Itakura, C., and Taketo, M. (1995). Loss of *Apc* heterozygosity and abnormal tissue building in nascent intestinal polyps in mice carrying a truncated *Apc* gene. Proc. Natl. Acad. Sci. USA *92*, 4482–4486.

Oshima, H., Oshima, M., Kobayashi, M., Tsutsumi, M., and Taketo, M.M. (1997). Morphological and molecular processes of polyp formation in Apc(delta716) knockout mice. Cancer Res. *57*, 1644–1649.

Otwinowski, Z., and Minor, W. (1997). Processing of X-ray diffraction data collected in oscillation mode. Methods Enzymol. *276*, 307–326.

Paronetto, M.P., Achsel, T., Massiello, A., Chalfant, C.E., and Sette, C. (2007). The RNA-binding protein Sam68 modulates the alternative splicing of Bcl-x. J. Cell Biol. *176*, 929–939.

Peifer, M., Berg, S., and Reynolds, A.B. (1994). A repeating amino acid motif shared by proteins with diverse cellular roles. Cell *76*, 789–791.

Polakis, P. (1995). Mutations in the *APC* gene and their implications for protein structure and function. Curr. Opin. Genet. Dev. *5*, 66–71.

Poy, F., Lepourcelet, M., Shivdasani, R.A., and Eck, M.J. (2001). Structure of a human Tcf4-β-catenin complex. Nat. Struct. Biol. *8*, 1053–1057.

Richard, S., Yu, D., Blumer, K.J., Hausladen, D., Olszowy, M.W., Connelly, P.A., and Shaw, A.S. (1995). Association of p62, a multifunctional SH2- and SH3-domain-binding protein, with src family tyrosine kinases, Grb2, and phospholipase C γ-1. Mol. Cell. Biol. *15*, 186–197.

Rubinfeld, B., Souza, B., Albert, I., Müller, O., Chamberlain, S.H., Masiarz, F.R., Munemitsu, S., and Polakis, P. (1993). Association of the APC gene product with β-catenin. Science *262*, 1731–1734.

Sampietro, J., Dahlberg, C.L., Cho, U.S., Hinds, T.R., Kimelman, D., and Xu, W. (2006). Crystal structure of a β-catenin/BCL9/Tcf4 complex. Mol. Cell *24*, 293–300.

Seeling, J.M., Miller, J.R., Gil, R., Moon, R.T., White, R., and Virshup, D.M. (1999). Regulation of β-catenin signaling by the B56 subunit of protein phosphatase 2A. Science *283*, 2089–2091.

Smits, R., Kielman, M.F., Breukel, C., Zurcher, C., Neufeld, K., Jagmohan-Changur, S., Hofland, N., van Dijk, J., White, R., Edelmann, W., et al. (1999). Apc1638T: a mouse model delineating critical domains of the adenomatous polyposis coli protein involved in tumorigenesis and development. Genes Dev. *13*, 1309–1321.

Stella, A., Montera, M., Resta, N., Marchese, C., Susca, F., Gentile, M., Romio, L., Pilia, S., Prete, F., Mareni, C., et al. (1994). Four novel mutations of the APC (adenomatous polyposis coli) gene in FAP patients. Hum. Mol. Genet. *3*, 1687–1688.

Su, L.K., Vogelstein, B., and Kinzler, K.W. (1993). Association of the APC tumor suppressor protein with catenins. Science *262*, 1734–1737.

Sun, J., and Weis, W.I. (2011). Biochemical and structural characterization of β-catenin interactions with nonphosphorylated and CK2-phosphorylated Lef-1. J. Mol. Biol. *405*, 519–530.

Taylor, S.J., and Shalloway, D. (1994). An RNA-binding protein associated with Src through its SH2 and SH3 domains in mitosis. Nature *368*, 867–871.

Terwilliger, T.C. (2000). Maximum-likelihood density modification. Acta Crystallogr. D Biol. Crystallogr. *56*, 965–972.

Terwilliger, T.C., and Berendzen, J. (1999). Automated MAD and MIR structure solution. Acta Crystallogr. D Biol. Crystallogr. *55*, 849–861.

Watanabe, T., Wang, S., Noritake, J., Sato, K., Fukata, M., Takefuji, M., Nakagawa, M., Izumi, N., Akiyama, T., and Kaibuchi, K. (2004). Interaction with IQGAP1 links APC to Rac1, Cdc42, and actin filaments during cell polarization and migration. Dev. Cell *7*, 871–883.

Wiseman, T., Williston, S., Brandts, J.F., and Lin, L.N. (1989). Rapid measurement of binding constants and heats of binding using a new titration calorimeter. Anal. Biochem. *179*, 131–137.

Wu, G., Wu, W., Hegde, M., Fawkner, M., Chong, B., Love, D., Su, L.K., Lynch, P., Snow, K., and Richards, C.S. (2001). Detection of sequence variations in the adenomatous polyposis coli (APC) gene using denaturing high-performance liquid chromatography. Genet. Test. *5*, 281–290.

Xing, Y., Clements, W.K., Le Trong, I., Hinds, T.R., Stenkamp, R., Kimelman, D., and Xu, W. (2004). Crystal structure of a β-catenin/APC complex reveals a critical role for APC phosphorylation in APC function. Mol. Cell *15*, 523–533.

Yabuki, T., Motoda, Y., Hanada, K., Nunokawa, E., Saito, M., Seki, E., Inoue, M., Kigawa, T., and Yokoyama, S. (2007). A robust two-step PCR method of template DNA production for high-throughput cell-free protein synthesis. J. Struct. Funct. Genomics *8*, 173–191.

FEBS Letters 585 (2011) 3452–3456

FEBS Letters

journal homepage: www.FEBSLetters.org

Cluster-forming property correlated with hemolytic activity by staphylococcal γ-hemolysin transmembrane pores

Noriko Tomita [a,*], Kazuyo Abe [a], Yoshiyuki Kamio [b], Makoto Ohta [a]

[a] Institute of Fluid Science, Tohoku University, Sendai, Miyagi, Japan
[b] Department of Biomechanical Engineering, Graduate School of Science and Engineering, Yamagata University, Yonezawa, Yamagata, Japan

ARTICLE INFO

Article history:
Received 6 September 2011
Revised 30 September 2011
Accepted 30 September 2011
Available online 12 October 2011

Edited by Peter Brzezinski

Keywords:
Staphylococcal γ-hemolysin
Two-component cytolysin
Pore-forming toxin
Cluster formation
Transmission electron microscopy
Image analysis

ABSTRACT

Staphylococcal γ-hemolysin (Hlg) is a pore-forming toxin consisting of two separate components, LukF (34 kDa) and Hlg2 (32 kDa). Here we show that Hlg pores aggregate and form clusters on human erythrocyte membranes in association with increasing hemolytic activity. Quantitative analysis using transmission electron microscopy and image processing revealed that the formation of single pores and clusters is related to the release of potassium ions and of hemoglobin from erythrocytes, respectively. This is the first study to suggest a novel and unique property which can facilitate hemolysis by the cluster formation of Hlg pores.

1. Introduction

Staphylococcal γ-hemolysin (Hlg) is a two-component cytolysin isolated from the culture fluid of *Staphylococcus aureus* [1,2]. It consists of Hlg (34 kDa) and Hlg2 (32 kDa), which cooperatively lyse erythrocytes of human and other mammalian species. Previous studies have shown that Hlg shares one component with the staphylococcal bi-component leukocytolytic toxin, leukocidin (i.e., Hlg1 is identical to LukF) [3,4]. Hence, Hlg1 is referred to as LukF.

We have studied the assembly and pore-forming nature of these toxins [5–10] and revealed that Hlg and Luk form a transmembrane pore with a functional diameter of ca. 2 nm [5,6]. Here, we suggest a novel and unique property of the Hlg pore. Transmission electron microscopy (TEM) observation of Hlg-treated human erythrocyte membranes revealed firstly that Hlg pores gather and form aggregates termed clusters on the membrane. Although aggregation of pores with alignment on the lipid vesicle have been reported in several pore-forming toxins such as α-hemolysin from *S. aureus* [11] and ClyA from *Escherichia coli* [12], a cluster-like structure aggregated by Hlg pores with random accumulation and localization on the erythrocyte membrane have not been found. Nguyen et al. have estimated cluster formation of Hlg pores based on the results by single-molecule fluorescence imaging [13] and our TEM observation (data not shown). Yamaji-Hasegawa et al. have shown that lysenin derived from the earthworm *Eisenia foetida*, which is known as a sphingomyelin-specific binding protein, has a property of aggregation on erythrocyte membranes [14]. However, in both studies, clusters aggregated with pores were not visualized directly and the correlation between the hemolytic activity and cluster formation was not investigated. The present study shows that the formation of clusters of Hlg pores and that a correlation of hemolytic activity to the cluster formation by counting with TEM. The results exhibit a latent property of Hlg for hemolysis with novel and unique mechanisms.

2. Materials and methods

2.1. Staphylococcal Hlg and hemolytic assay

LukF and Hlg2 were purified from the culture supernatant of *S. aureus* 5R Smith strain as mature protein without signal peptide following reference [3]. Accession numbers (AN) of LukF and Hlg2 from *S. aureus* 5R Smith strain are not registered yet. However, both nucleotide sequences were already determined [4] and they

Abbreviations: Hlg, staphylococcal γ-hemolysin; LukF, LukF (Hlg1) component of staphylococcal γ-hemolysin; Hlg2, Hlg2 component of staphylococcal γ-hemolysin; TEM, transmission electron microscopy

* Corresponding author. Address: Institute of Fluid Science, Tohoku University, 2-1-1 Katahira, Aoba-ku, Sendai, Miyagi 980-8577, Japan. Fax: +81 22 217 5309.
E-mail address: tomita@ifs.biofluid.tohoku.ac.jp (N. Tomita).

0014-5793/$36.00 © 2011 Federation of European Biochemical Societies. Published by Elsevier B.V. All rights reserved.
doi:10.1016/j.febslet.2011.09.041

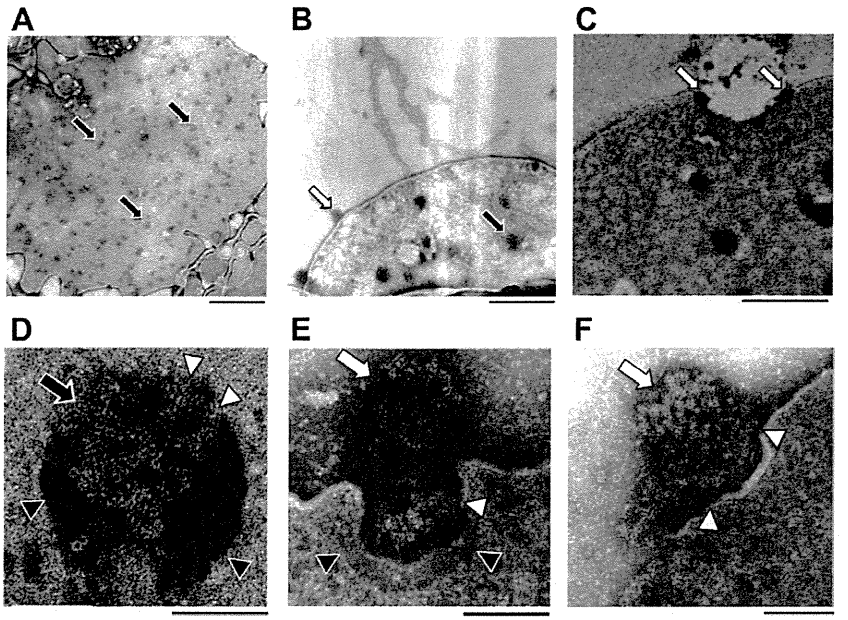

Fig. 1. TEM images of the clusters formed on the Hlg-treated HE membranes HEs were incubated with LukF (A: 150 pM, B–F: 30 pM) and Hlg2 (A: 150 pM, B–F: 30 pM) at 37 °C for 30 min. Black arrowheads mark the edge of the hole around the clusters. White arrowheads show the pores anchored to the membranes. Scale bars in panels A–C and D–F shows 500 and 100 μm, respectively.

are same as those from *S. aureus* N315 strain. Please refer the AN of LukF (NP_375532) and Hlg2 (NP_375530) from N315 strain. Human erythrocytes (5×10^7 cells/ml, HEs) were incubated with 20 pM of LukF and Hlg2 at 0 °C for 1 min. The erythrocytes were collected by centrifugation at 2000×*g* for 1 min at 4 °C and washed twice with phosphate buffered saline to remove non-bound Hlg. The Hlg-bound HEs were incubated at 37 °C for 1, 3, 5, 10 and 20 min. After centrifugation at 800×*g* for 5 min, hemolytic activity, that is the amount of hemoglobin released from the Hlg-bound erythrocytes, was measured with absorbance at 541 nm for the supernatants. One hundred percent hemolysis was defined as the absorbance value obtained when erythrocytes were exposed to 0.5% Triton X-100 at 37 °C for 20 min. Zero percent hemolysis was defined as the absorbance value obtained when the cells were incubated without toxin at 0 °C for 5 min.

2.2. Efflux of potassium ions from Hlg-treated HE

HEs were incubated with 20 pM of LukF and Hlg2 at 0 °C for 1 min. Removal of non-bound Hlg and incubation were performed as described in Section 2.1. The amount of potassium ions from the Hlg-treated erythrocytes was measured as described previously [5].

2.3. TEM observation

The samples for TEM were prepared as follows. (i) HEs were incubated with 30–150 pM of LukF and Hlg2 at 37 °C for 30 min. Erythrocyte membranes were collected by centrifugation at 15,000×*g* at 4 °C for 5 min and washed twice with 5 mM sodium phosphate buffer (pH 7.4) by centrifugation (this method is applied to the experiment shown in Fig. 1). (ii) HEs were treated with Hlg as described in Section 2.1. Membranes were collected and washed as described above (this method is applied in the experiments as shown in Figs. 2–5).

The TEM observation of the specimens stained negatively with 1% (w/v) sodium phosphotungstic acid, as described previously [7], was performed under a Hitachi electron microscope H-8100 (Hitachi, Tokyo). The number of pores and that of clusters in the field were converted to the number per cell, the total surface area of the erythrocyte being 160 μm^2. Pores existed as single entities and formation of all clusters per cell were defined as a single pore and a clustered pore, respectively. The number of clustered pores and the total number of pores per cell were calculated as follows:

$$\text{Clustered pores/cell} = (\text{the number of clusters/cell}) \times (\text{the number of pores from the top view/cluster}) \quad (1)$$

$$\text{Total number of pores/cell} = \text{clustered pores/cell} + \text{single pores/cell} \quad (2)$$

All numbers were counted in 20–30 fields in three independent experiments in each condition.

2.4. Image analysis

HEs were treated with 30–300 pM of LukF and Hlg2 and washed as described in Section 2.1. The cluster formation being observed as described in Section 2.3. The clusters located on the membrane were extracted using a threshold of concentration value of the images with Scion Image Beta 4.03. The area of each cluster was calculated from the number of pixels in the region of the cluster.

2.5. Statistics

The Tukey–Kramer method was used to compare the means of the number of pores per cluster and those of the number of clusters per cell for 5, 10 and 20 min (Fig. 4A and B). The Mann–Whitney U test was used to compare means of the top and side areas per cluster between 3 and 30 min (Fig. 5A). The Kruskal–Wallis test was used to compare the means of the top and the side areas per cluster in three toxin concentrations (Fig. 5B). The level of statistical significance used was $P < 0.05$.

3. Results and discussion

3.1. The Hlg pore complexes form clusters on the cell membrane of HEs

Fig. 1 shows typical TEM images of Hlg-treated HEs. In this condition, the hemolytic activity reaches almost 100% (data not

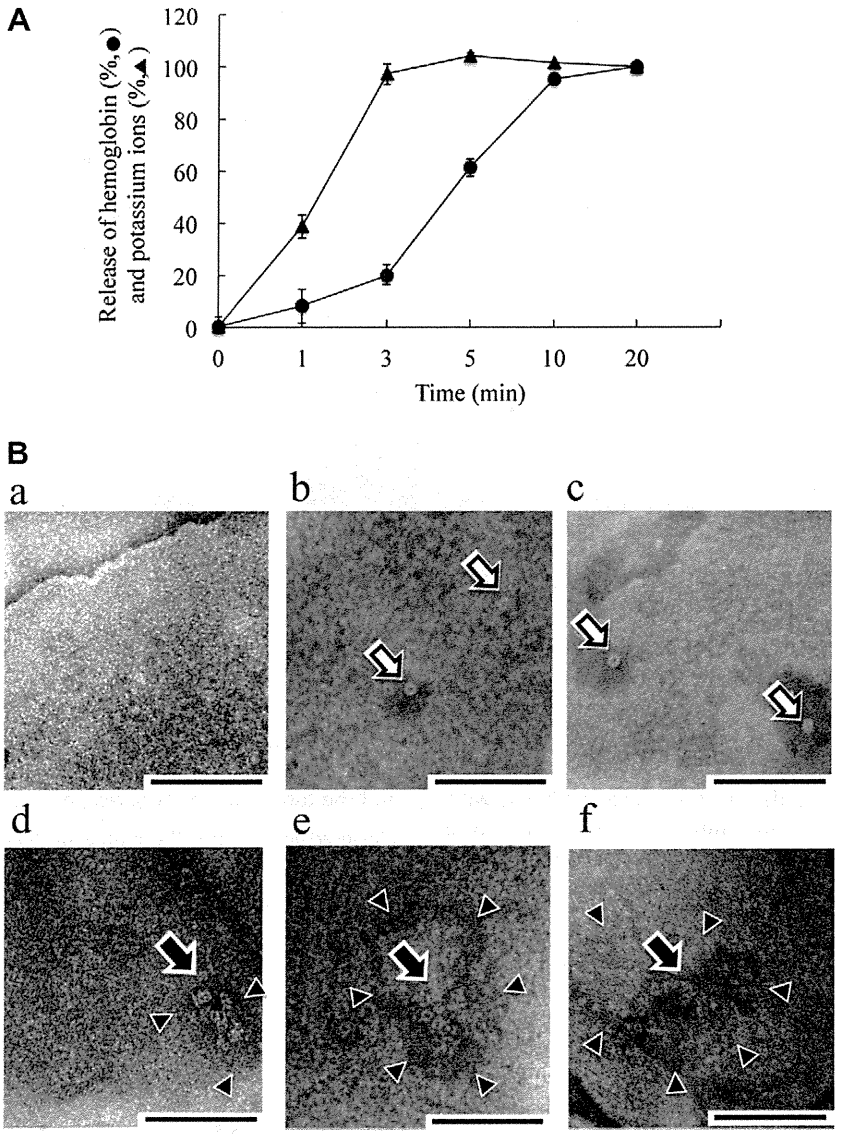

Fig. 2. Hlg-induced releases of the hemoglobin and the potassium ion correlated with the formation of clusters and single pores. (A) Releases of the hemoglobin and the potassium ions with time. Before incubation at 37 °C each time, the erythrocytes were incubated with LukF (20 pM) and Hlg2 (20 pM) at 0 °C for 1 min and washed to remove unbound toxin. (B) Formation of single pores and clusters on the Hlg-treated erythrocytes with time. Panels a–f are typical images at the points of 0, 1, 3, 5, 10 and 20 min, respectively, shown in Fig. 2A. White and black arrows indicate typical single pores and clusters, respectively. Black arrowheads mark the edge of the hole around clusters. Scale bars show 100 μm.

shown). In panels A, B and C, the contrast-enhanced portions show aggregations of pores with top and side views. In this study, an aggregation of pores was termed a cluster. In panel C, the membrane region between two clusters indicated by white arrows is caved in. Panels D, E and F are enlarged images of the clusters. Panel D shows the top view of the cluster (black arrow), and panels E and F are side views of the clusters (white arrows). The pores forming the clusters are often piled up three-dimensionally in various directions as shown by white arrows in panels B, C, E and F. As shown by black arrowheads in panels D and E, the membranes around the clusters disappear and large holes with diameters of a few hundred nanometers are formed. As shown by white arrowheads, several pores in the cluster are anchored to a part of the membrane. In our previous study, the diameter of Hlg pores was estimated to be approximately 2 nm [5], which is smaller than that of hemoglobin. However, hemoglobin seems to easily pass through the large hole around the cluster.

Fig. 2 shows that the release of potassium ions and hemoglobin from HEs and the formation of single pores and clusters with time. In this condition, each assay can be monitored under a constant amount of toxin bound to the erythrocyte. The concentrations of 20 pM of LukF and Hlg2 are enough to form single pores and clusters. As shown in Fig. 2A, almost all potassium ions in the erythrocyte are leaked within 3 min. In contrast, only 20% of hemoglobin in the erythrocyte is leaked in 3 min. Representative TEM images show the pores existed as single entities mainly for 3 min (Fig. 2B, panels b and c), and the clusters appeared after 5 min (Fig. 2B, panels d–f). With time, the membranes on the cluster are destroyed (shown with black arrowheads in Fig. 2B, panels d–f). These results could indicate that potassium ions inside the erythrocyte can pass through the single pores and that the hemoglobin can easily pass through after a large hole is formed around the cluster. The breakage of the membrane around the cluster is still unknown, and further studies are necessary to resolve a mechanism of the formation of a large hole. As a hypothesis, it may be caused by the concentrative influx of water and ion molecules through the cluster and/or the loss of flexibility of the membrane. The quantity of the release of hemoglobin observed within 3 min